land

Article

Comparative Analysis of Photosynthetically Active Radiation Models Based on Radiometric Attributes in Mainland Spain

Ousmane Wane [1,2,3], Julián A. Ramírez Ceballos [1,*], Francisco Ferrera-Cobos [1], Ana A. Navarro [1], Rita X. Valenzuela [1] and Luis F. Zarzalejo [1]

[1] CIEMAT Energy Department, Renewable Energy Division, Avda. Complutense 40, 28040 Madrid, Spain
[2] E.T.S.I. Agronómica, Alimentaria y de Biosistemas, Universidad Politécnica de Madrid, Avda. Puerta Hierro 2-4, 28040 Madrid, Spain
[3] Microbial and Plant Biotechnology Department, Centro de Investigaciones Biológicas Margarita Salas-CSIC, Ramiro de Maetzu 9, 28040 Madrid, Spain
* Correspondence: jaramirezce@gmail.com; Tel.: +34-91-346-6668

Abstract: The aims of this work are to present an analysis of quality solar radiation data and develop several hourly models of photosynthetically active radiation (PAR) using combinations of radiometric variables such as global horizontal irradiance (GHI), diffuse horizontal irradiance (DHI), and direct normal irradiance (DNI) from their dimensionless indices atmospheric clearness index (k_t), horizontal diffuse fraction (k_d), and normal direct fraction (k_b) together with solar elevation angle (α). GHI, DHI, and DNI data with 1-minute frequencies in the period from 2016 to 2021 from CEDER-CIEMAT, in a northern plateau, and PSA-CIEMAT in the southeast of the Iberian Peninsula, were used to compare two locations with very different climates according to the Köppen—Geiger classification. A total of 15 multilinear models were fitted and validated (with independent training and validation data) using first the whole dataset and then by k_t intervals. In most cases, models including the clearness index showed better performance, and among them, models that also use the solar elevation angle as a variable obtained remarkable results. Additionally, according to the statistical validation, these models presented good results when they were compared with models in the bibliography. Finally, the model validation statistics indicate a better performance of the interval models than the complete models.

Keywords: photosynthetically active radiation; clearness index; solar elevation; PAR modeling

check for updates

Citation: Wane, O.; Ramírez Ceballos, J.A.; Ferrera-Cobos, F.; Navarro, A.A.; Valenzuela, R.X.; Zarzalejo, L.F. Comparative Analysis of Photosynthetically Active Radiation Models Based on Radiometric Attributes in Mainland Spain. *Land* **2022**, *11*, 1868. https://doi.org/10.3390/land11101868

Academic Editor: Adrianos Retalis

Received: 15 September 2022
Accepted: 17 October 2022
Published: 21 October 2022

1. Introduction

Plants and other living organisms, such as algae, perform photosynthesis to convert solar energy into chemical energy that they can use in their metabolism processes. The portion of solar spectra they use for photosynthesis is called photosynthetically active radiation (PAR), which is located between 400 and 700 nm in wavelength. PAR is an agro-meteorological parameter with multiple applications in many fields, such as the agro-food industry or crop culture. These visible spectral measurements constitute a fundamental factor in the metabolism, growth, and biomass production of plants or crops [1–7] and evaluate CO_2 sequestration by microalgae [8–10]. This variable is also of interest in calculations that involve gross or net primary production [11,12], the efficiency of using PAR to convert absorbed energy into biomass [13], or carbon exchange between the ecosystem and the atmosphere [14,15]. For example, the optical properties covering between 400 and 700 nm of the greenhouse must be taken into account in the design of it [16,17], as well as the availability of PAR within the greenhouse, which seems to be highly affected in the vertical plane by its orientations [18].

Due to the complexity of interactions with the Earth's atmosphere, the spatial and seasonal variability of solar irradiance, particularly at the PAR spectrum, has been addressed in previous studies [19–21]. Furthermore, the ratio between PAR and global irradiance also shows seasonal changes and spatial variability worldwide [22]. The amount of solar irradiance reaching the Earth's surface is affected by the cloudiness and aerosols present in the atmosphere [23]. The extinction of irradiance caused by aerosols is greater for shorter wavelengths, in consequence, the presence of aerosols affects the ultraviolet or visible bands more strongly than the infrared bands [24]. On the other hand, clouds affect solar irradiance by absorption and scattering, while the absorption of water vapor is higher at longer wavelengths, scattering is non-selective. Therefore, PAR, which is located in the visible range, is strongly dependent on the climatic and atmospheric conditions of each location [25,26] and is strongly affected by the presence of clouds, and higher values are measured under clear skies [27].

Radiometric or meteorological stations including PAR sensors are scarce. Global horizontal irradiance (GHI), diffuse horizontal irradiance (DHI), and direct normal irradiance (DNI) are the most frequently available measured solar radiation data. PAR data are not always available at a specific location or for a required period. To fill this gap, remote sensing data are necessary, such as satellite data or PAR models. In this context, many models have been developed in the past to provide PAR estimates at different locations. Therefore, many local PAR models based on empirical correlations between radiometric and meteorological parameters are described in the literature. Escobedo et al. (2009) developed several models correlating the GHI and PAR considering four sky conditions in terms of the daily values of clearness index (k_t) [28]; Alados et al. (1996) described the variation of the ratio of PAR to broadband solar radiation from multivariate models with other information such as (k_t), solar elevation angle (α), and dew point temperature [29]; Mizoguchi et al. (2014) proposed a multiple linear regression model with independent variables as k_t, optical air mass, and water vapor pressure [30]; Yu et al. (2015) predicted daily PAR from empirical relationships GHI, k_t and horizontal diffuse fraction (k_d), skylight brightness along with the dew point temperature and the cosine of the solar zenith angle [31]; Pashiardis et al. (2017) used to investigate the seasonal characteristics of the PAR and the PAR fraction according to the GHI, k_t, optical air mass, zenith solar angle, water vapor saturation pressure, and water vapor pressure [32]; Vindel et al. (2018) and Ferrera-Cobos et al. (2020) used the GHI to model PAR radiation [21,26]; Ferrera-Cobos et al. (2021) modelled climate regions using variables such as GHI, k_t, temperature, relative humidity, and zenith angle cosine [33]; and García-Rodríguez et al. (2021) used ten meteorological indices such as sky clearness index, k_d, horizontal direct fraction, GHI, zenith angle cosine, temperature, pressure, and others [34]. These PAR models generally use k_t, k_d, horizontal direct fraction, and/or other meteorological parameters but do not include the normal direct fraction (k_b) [35,36] as an input variable to the models. Liu and Jordan (1960) defined this index and established an empirical relationship between the intensities of direct and diffuse radiation on clear days [37].

In the present work, several PAR models are elaborated using combinations of radiometric variables such as GHI, diffuse horizontal irradiance (DHI), and direct normal irradiance (DNI) from their dimensionless parameters k_t, k_d, and k_b, along with α. The models were then validated at two stations located in the interior of the northern plateau, Centro de Desarrollo de Energías Renovables (CEDER-CIEMAT) and in the southeast of the Iberian Peninsula, Plataforma Solar de Almería (PSA-CIEMAT). Finally, the most remarkable models are compared with models in the bibliography.

2. Materials and Methods

Data from two radiometric stations located in Spain were used for this work, particularly CEDER-CIEMAT (41.60° N, 2.51° W and 1099 m.a.s.l.) in the center of the Iberian Peninsula and PSA-CIEMAT (37.09° N, 2.37° W and 496 m.a.s.l.) in the southeast of Spain (Figure 1). CEDER-CIEMAT has a continental Mediterranean climate, and PSA-CIEMAT has an arid climate according to the Köppen–Geiger classification [38,39]. Both stations provided GHI, DHI, and DNI data with 1-min frequencies in the period from 30 January

2018 to 13 July 2021 in the case of CEDER-CIEMAT, while PSA-CIEMAT provided data from 24 February 2016 to 13 July 2021.

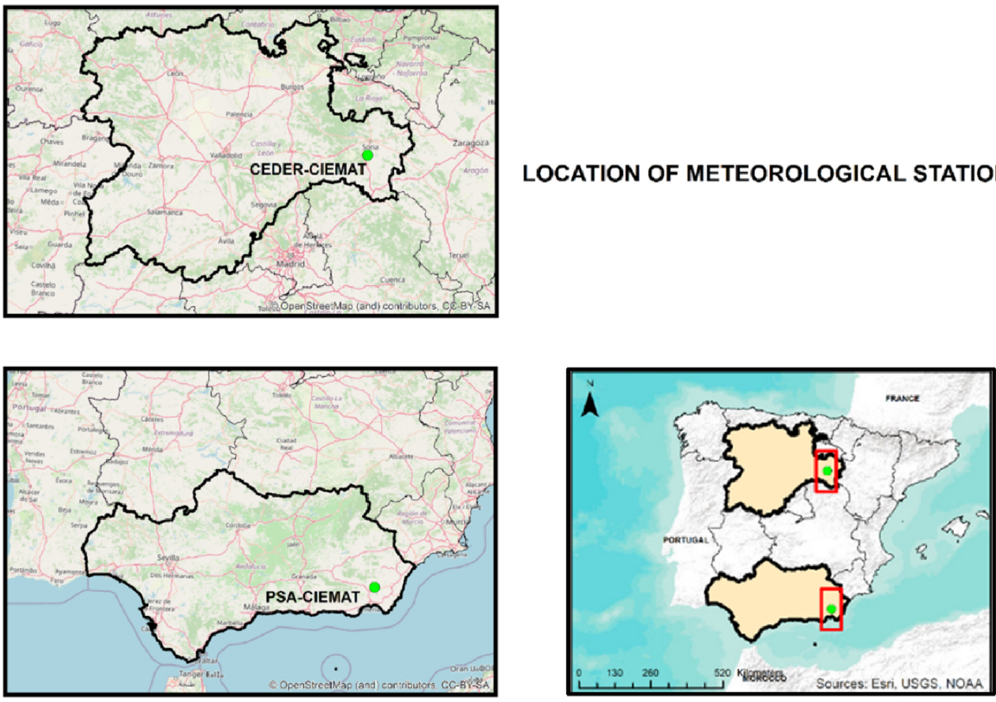

Figure 1. Location of the CEDER-CIEMAT and PSA-CIEMAT stations.

Kipp and Zonen CM-11 or CM-21 pyranometers, secondary-standard instruments, were used to measure the experimental data for GHI and DHI, while a first-class CH1 pyrheliometer was used to measure the experimental data for DNI. In every instance, these instruments comply with the requirements set forth by WMO (2008) for high-quality class sensors. The sensors are attached to a Kipp and Zonen 2AP two-axis tracker, which has an accuracy of better than 0.1° and tracks the Sun's path.

On the other hand, periodic calibration is carried out in accordance with ISO 9059, ISO 9846, and ISO 9847 in a specific calibration facility at PSA. These instruments have an accuracy of less than 2%.

Finally, PAR was collected using an ML-020P (EKO Instruments). There is no specific standard method for performing a calibration; usually, it is performed using standard light sources that are traceable to NIST, and thus a calibration is performed with the manufacturer every two years. The precision is ±5%.

To ensure data quality by minimizing the effect of environmental factors, the quality control method defined by the BSRN has been applied [40]. To date, no standard PAR quality control model has been defined. This led to several approaches to the validation of PAR data. However, in this work, PAR data have been validated using the following criteria [32,41]: the measured PAR values must be lower than the extraterrestrial PAR, and the daily PAR/GHI ratio should be in the range of 1.6 and 2.5 μmol/Ws. The second criterion is arbitrary and is based on a minimum number of possible outliers. In other words, by bounding the PAR/GHI ratio between 1.6 and 2.5, the number of outliers eliminated by the last filter is lower than for other intervals. Data recorded at night were deleted a priori.

Before generating the training dataset, data with a solar elevation angle of less than 7° were also eliminated to minimize measurement errors due to a large mass of air traversed when the sun is close to the horizon (solar geometry). In addition, the possible outliers present in each of the subsets were removed to eliminate the unrepresentative data [42]. After filtering, 80% of the randomly taken data from each database was used for model fitting, and the remaining 20% was used to validate it separately in each location. To avoid overweighting, the same number of observations was chosen for both databases to conduct the training of the models. As the PSA-CIEMAT dataset is larger than CEDER-CIEMAT, the validation data for PSA-CIEMAT would be composed of the initial 20% from the total measurement period plus the data belonging to the initial 80% that have not been used to fit the model. Therefore, the training data of the models are the union of those obtained from CEDER-CIEMAT and PSA-CIEMAT.

The explanatory variables of the model were calculated using the expressions of (1) to (4) [43,44], where I_{sc} is the extraterrestrial irradiance constant equal to 1367 Wm^{-2}. δ, ϕ, ω, and ε represent, respectively, the declination, the geographical latitude of the station, the solar hour angle, and eccentricity correction factor of the Earth's orbit [35,36,44].

$$\sin(\alpha) = \sin(\phi) \cdot \sin(\delta) + \cos(\phi) \cdot \cos(\delta) \cdot \cos(\omega) \quad (1)$$

$$k_t = \frac{GHI}{I_{SC} \cdot \varepsilon \cdot \sin(\alpha)} \quad (2)$$

$$k_d = \frac{DHI}{GHI} \quad (3)$$

$$k_b = \frac{DNI}{I_{SC} \cdot \varepsilon} \quad (4)$$

The models were developed through multilinear regressions using different combinations of the variables k_t, k_d, k_b, and $\sin(\alpha)$. The number of possible combinations was 15; that is, $2^n - 1$ models, where n is the number of independent variables listed above. These independent variables of the models are dimensionless. Taking into account that the magnitude range of the independent variables and the PAR is very different, the PAR/I_0 ratio was chosen as the output variable for the models tested, where I_0 is the extraterrestrial irradiance for 1 h centered around the middle of each hour angle ω [44].

$$I_0 = I_{sc} \cdot \varepsilon \cdot \sin(\alpha) \quad (5)$$

The complete models were trained from the entire training dataset, while the interval models were fitted from the interval-separated training data. The training and validation data used for the complete model are the same as those used for the corresponding interval model. In the latter case, the training and validation data were divided into three k_t intervals to accommodate different sky conditions, so that the first interval ($0 \leq k_t \leq 0.3$) corresponds to cloudy skies, the second ($0.3 < k_t \leq 0.7$) to partly cloudy skies, while the third ($0.7 < k_t \leq 1$) refers to clear sky conditions [31,45]. To assess the goodness of the models, the PAR estimated from the three intervals was unified before validation. The models were validated by comparing the PAR estimates with the 20% measured data (validation data). The same was performed for the complete models. Statistical parameters such as the coefficient of determination (R^2), mean bias error (MBE), mean absolute error (MAE), root mean square error (RMSE), mean percentage error (MPE), and absolute error were used to assess the goodness of all models:

$$MBE = \frac{1}{n}\sum_{i=1}^{n}(PAR_{Modeled} - PAR_{Measured}) \quad (6)$$

$$MAE = \frac{1}{n}\sum_{i=1}^{n}|PAR_{Modeled} - PAR_{Measured}| \quad (7)$$

$$RMSE = \sqrt{\frac{1}{n}\sum_{i=1}^{n}(PAR_{Modeled} - PAR_{Measured})^2} \quad (8)$$

$$MPE = \frac{100\%}{n}\sum_{i=1}^{n}\frac{PAR_{Measured} - PAR_{Modeled}}{PAR_{Measured}} \quad (9)$$

$$R^2 = \frac{\sigma^2_{PARmodeled\ PARmeasured}}{\sigma^2_{PARmodeled}\ \sigma^2_{PARmeasured}} \tag{10}$$

$$\text{Absolute\_error} = \text{measured\_value} - \text{estimated\_value} \tag{11}$$

3. Results and Discussion

3.1. Graphical Analysis of PAR and Other Radiometric Variables

The graphs illustrated in Figures 2–7 show the behavior of PAR with respect to the other radiometric variables, using previously filtered data provided by both stations.

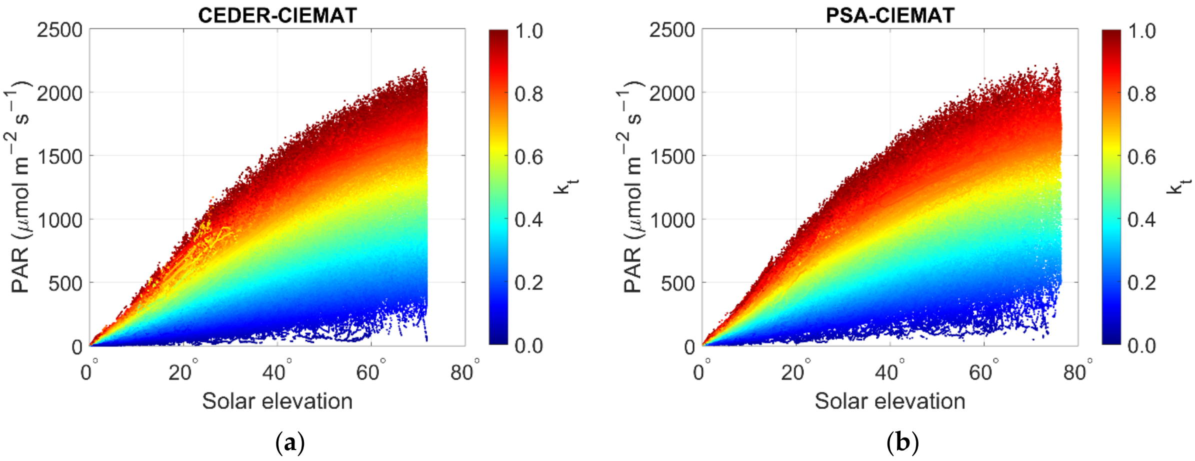

Figure 2. Scatterplot between PAR and solar elevation angle. The color bar represents the clearness index. (**a**) CEDER-CIEMAT station; (**b**) PSA-CIEMAT station.

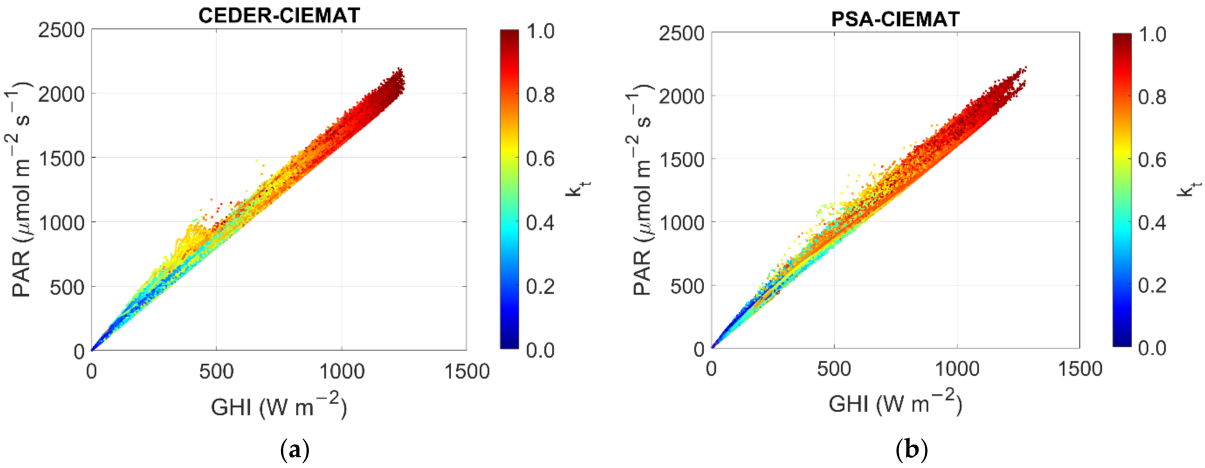

Figure 3. Scatterplot between PAR and GHI. The color bar represents the clearness index. (**a**) CEDER-CIEMAT station; (**b**) PSA-CIEMAT station.

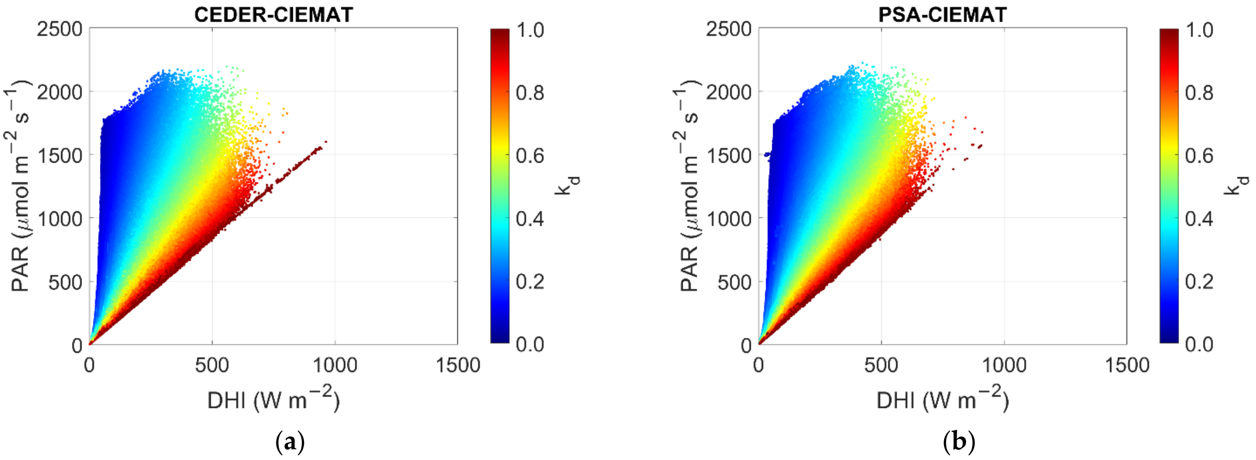

Figure 4. Scatterplot between PAR and DHI. The color bar represents the k_d index. (**a**) CEDER-CIEMAT station; (**b**) PSA-CIEMAT station.

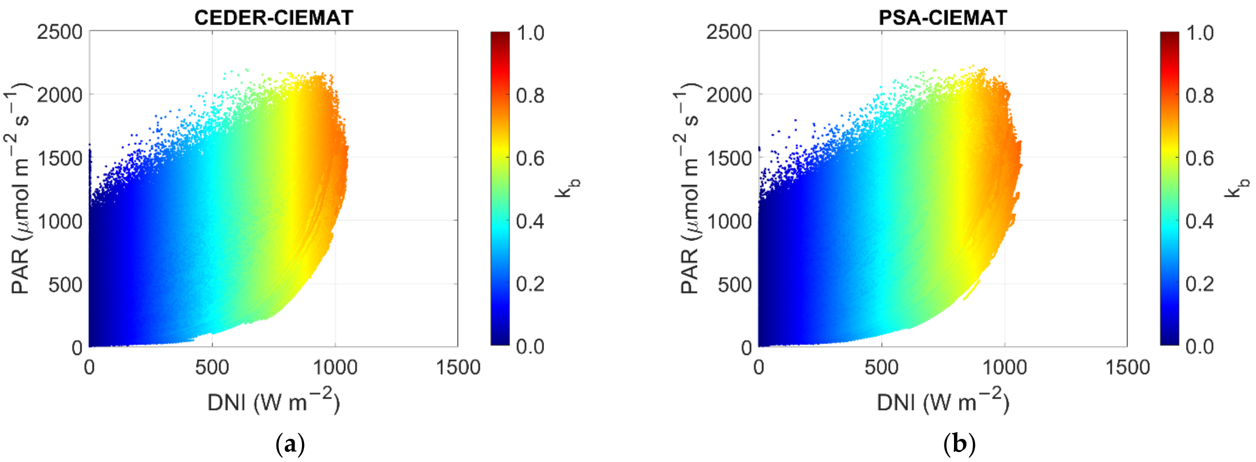

Figure 5. Scatterplot between PAR and DNI. The color bar represents the k_b index. (**a**) CEDER-CIEMAT station; (**b**) PSA-CIEMAT station.

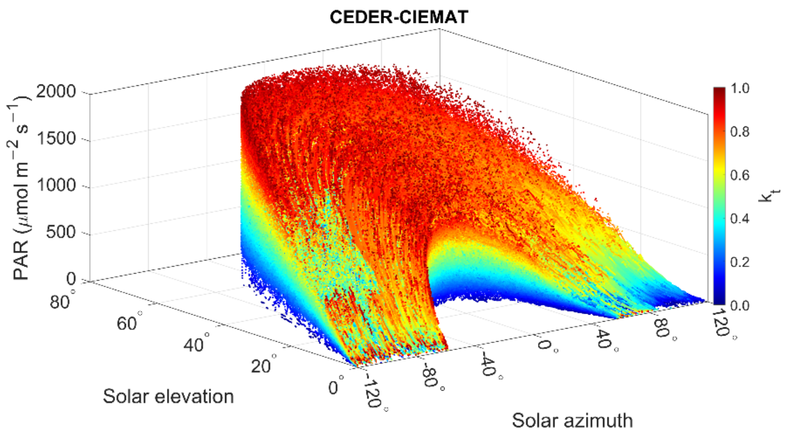

Figure 6. Scatter plot between PAR, solar elevation angle, and solar azimuth angle for the CEDER-CIEMAT station (where the positive azimuth angle indicates the morning hours). The color bar represents the clearness index.

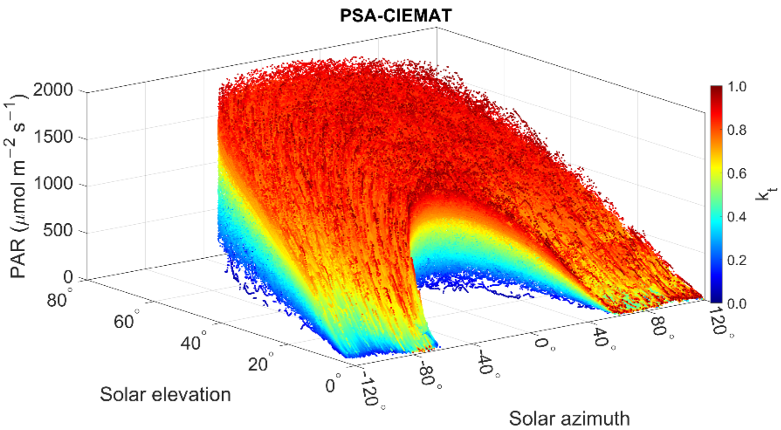

Figure 7. Scatter plot between PAR, solar elevation angle, and solar azimuth angle for the PSA-CIEMAT station (where the positive azimuth angle indicates the morning hours). The color bar represents the clearness index.

In the plots shown in Figure 2, the scatterplot between the PAR and the solar elevation angle is illustrated. As expected, higher PAR values were reached for higher solar elevation angles and with high clearness indices. In fact, the difference between clear days (k_t higher than 0.7) and cloudy days (k_t lower than 0.3) is very clear at both stations. However, there are some particularities in each station. For instance, since PSA-CIEMAT is in a more southern location, there were larger solar elevation angles there. On the other hand, in CEDER-CIEMAT, lower clearness indexes were reached for solar elevation angles below 30°. This can also be seen in Figure 6, which will be commented on below.

In Figure 3, a considerable number of high values of k_t are observed over a wide range of irradiance in the PSA-CIEMAT station than in the CEDER-CIEMAT station (Figure 3a,b). This can be explained by the arid climate present in this southern part of Spain, which typically implies cloudless conditions and scarce precipitations. In addition, Figure 3 depicts that there is a small dispersion between GHI and PAR, allowing to appreciate the linear dependence of these two variables. Nevertheless, the graphs of both stations show a certain dispersion that can be related to the different sensitivities and the aging of the sensors.

In Figure 4, the scatterplot between PAR and DHI reveals similar trends at both stations. On clear days (k_d lower than 0.3), low DHI corresponded to high PAR values, and the opposite occurred on cloudy days (k_d higher than 0.7). In CEDER-CIEMAT, higher DHI values were observed (Figure 4a). This result is a consequence of the continental Mediterranean climate present in this station, where there are more cloudy or stormy days than in the arid climate of PSA-CIEMAT (Figure 4b).

Similarly, Figure 5 shows similar trends in both stations in the scatterplots between the PAR and DNI. The main difference between both stations is that on cloudy days (k_b lower than 0.3 and DNI close to zero), higher PAR values were reached in CEDER-CIEMAT.

Some features of cloud cover and the general conditions of each station can be drowned out in Figures 6 and 7. As can be seen in both figures, in CEDER-CIEMAT, the cloudiest conditions occurred mostly in the morning (positive azimuth angle). The lack of clear conditions during the afternoon (negative azimuth angle) is also noticeable during some periods of the year at CEDER-CIEMAT. However, in PSA-CIEMAT, the cloudiest conditions occurred early in the late afternoon. From these two figures, it can be seen that there are missing data at very low solar elevation angles (sunrise and sunset). These data were removed when applying the different filters. Considered as outliers, their elimination may be caused by the progressive disappearance of the solar disc on the horizon of the measuring instrument.

Looking at the graphs shown in Figures 2–7, it can be seen that the mathematical relationship between the PAR and the other variables varies as the k_t, k_d, k_b, or α indexes vary. This variation indicates that, for PAR modeling, it is necessary to use a combination of these variables. The models listed in Table 1 were chosen to be tested in this work.

The main trends of the relationship between PAR and the other variables were common in both stations. Although they are located in places with different climates (continental Mediterranean in CEDER-CIEMAT and arid in PSA-CIEMAT [38,39]), the main characteristics of these climates are not different enough to cause a significant difference in the PAR behavior. However, some particularities were observed at each station. For example, the highest solar elevation angles were reached at the PSA-CIEMAT station, and the highest k_t values were also observed at this station. In CEDER-CIEMAT, higher DHI and PAR values were obtained on cloudy days. The cloudiest conditions occurred early in the afternoon in PSA-CIEMAT, while in CEDER-CIEMAT, the cloudiest conditions occurred late in the morning. These particularities influence the dependence of the PAR on other radiometric parameters. In the different scattering plots carried out on all data measured and illustrated above, the relevant aspect of the interdependence between the PAR and the GHI can also be appreciated. However, it can be observed that this relationship is not perfectly linear. In addition, in the partially cloudy sky ($0.3 < k_t \leq 0.7$), a scattering is observed (Figure 3) that could come from the effects of the clouds or related to the different sensitivities and aging of the sensors. Outside of this partially cloudy sky interval, the two parameters show a more apparent correlation. The cause of an apparent correlation could be that two parameters are related to a third parameter, which led us to study and analyze various combinations in order to highlight the appropriate models.

3.2. Complete Models Development and Validation

Table 1 shows the fit parameters for each of the complete models presented. The selection of these models was made by excluding combinations that do not include $\sin(\alpha)$ as an explanatory variable, those that include only the term $\sin(\alpha)$, and those that include all variables. A graphical analysis, which we will present in the following sections, showed that the models that include the variables k_t or k_t and $\sin(\alpha)$ present more relevant correlation results with the validation data, while in the rest of the models, the dispersion is more notable (Figure 8). This table also includes the results of the application of the validation statistics to the different models.

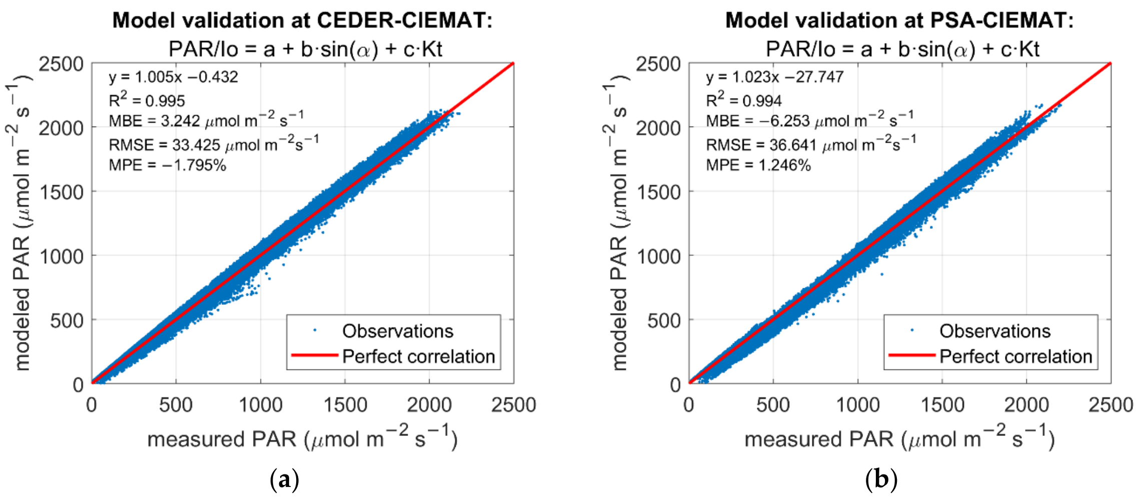

Figure 8. *Cont.*

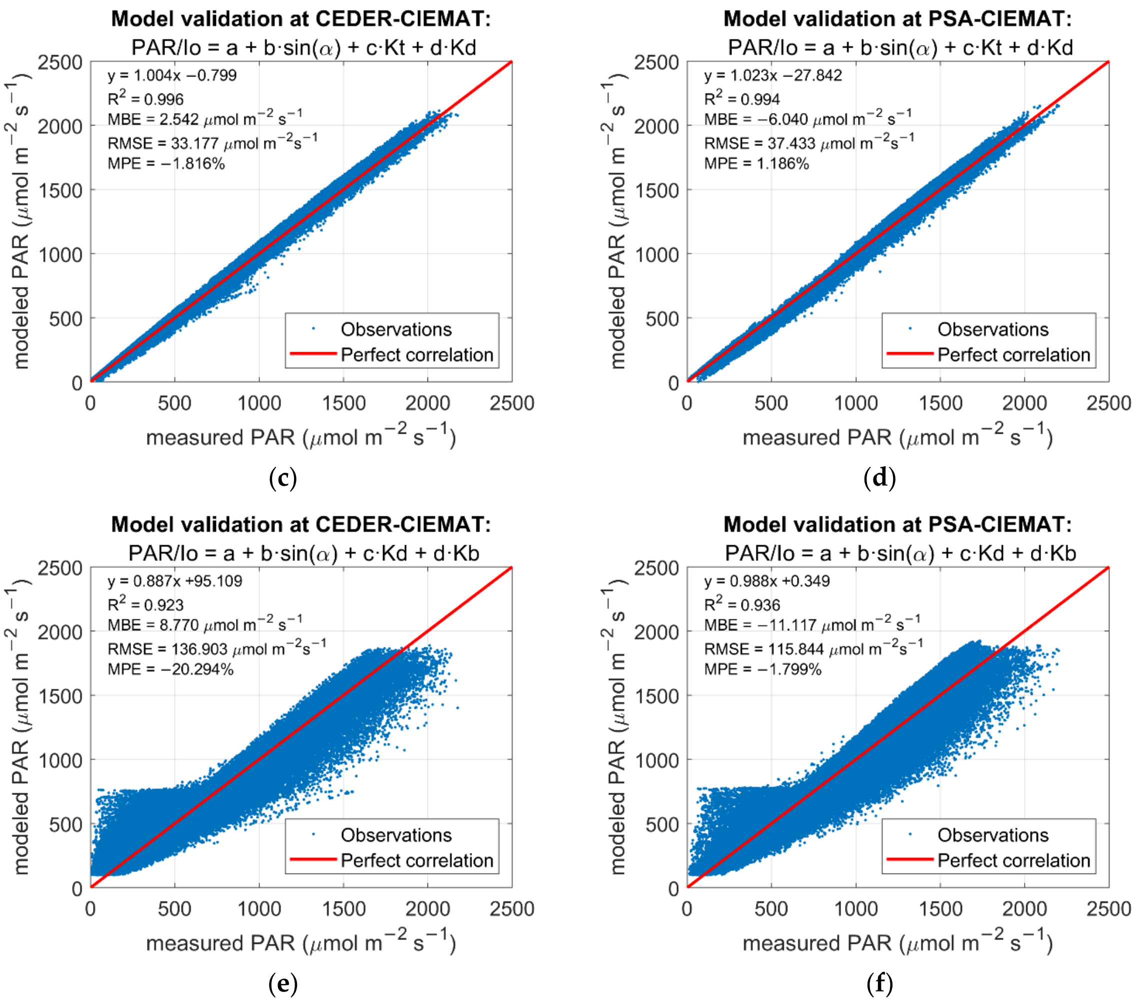

Figure 8. Results obtained in the validation of complete models indicated above, each graph using data measured in the CEDER-CIEMAT (**a**,**c**,**e**) and PSA-CIEMAT (**b**,**d**,**f**) stations.

From a qualitative point of view, the six models presented in Table 1 can be divided into two groups: those that consider only two independent variables (m_1, m_2, and m_3) and those that use three (m_4, m_5, and m_6). This classification is not significant with respect to the results obtained; however, we appreciate that there are notable differences in a classification with respect to the explanatory variables considered:

- G1: models that include $\sin(\alpha)$ and k_t (m_1, m_4, and m_5),

$$\text{m\_1: } \frac{PAR}{I_0} = a + b \cdot \sin(\alpha) + c \cdot k_t$$
$$\text{m\_4: } \frac{PAR}{I_0} = a + b \cdot \sin(\alpha) + c \cdot k_t + d \cdot k_d$$
$$\text{m\_5: } \frac{PAR}{I_0} = a + b \cdot \sin(\alpha) + c \cdot k_t + d \cdot k_b$$

- G2: models that do not include sin (α) and k_t simultaneously (m_2, m_3, and m_6),

$$\text{m\_2: } \frac{PAR}{I_0} = a + b \cdot \sin(\alpha) + c \cdot k_d$$
$$\text{m\_3: } \frac{PAR}{I_0} = a + b \cdot \sin(\alpha) + c \cdot k_b$$
$$\text{m\_6: } \frac{PAR}{I_0} = a + b \cdot \sin(\alpha) + c \cdot k_d + d \cdot k_b$$

The RMSE comparison allows us to appreciate the difference in the order of magnitude between those of G1 and those of G2. The RMSEs of G1 are between 33.177 and 37.433 μmol m^{-1} s^{-1}, while those of G2 are between 115.844 and 145.848 μmol m^{-1} s^{-1} (Table 1). Regarding the G1 group, it can be seen that validation with the CEDER data provides a lower RMSE value than that obtained with the PSA data. On the other hand, it can be seen that for G2, the RMSE is higher with the CEDER data.

Table 1. Results obtained from the fits of six complete models of groups G1 and G2 and their validation statistics.

Models		a	b	c	d	Station	MAE [1]	MBE [1]	RMSE [1]	MPE (%)	R^2
G1	m_1	0.018	−0.030	0.385	-	CEDER PSA	25.683 28.445	3.242 −6.253	33.425 36.641	−1.795 1.246	0.995 0.994
	m_4	0.028	−0.029	0.373	−0.008	CEDER PSA	25.313 28.913	2.542 −6.040	33.177 37.433	−1.816 1.186	0.996 0.994
	m_5	0.019	−0.030	0.380	0.004	CEDER PSA	25.595 28.673	2.990 −6.152	33.360 36.979	−1.851 1.226	0.995 0.994
G2	m_2	0.295	0.035	−0.198	-	CEDER PSA	108.033 92.002	6.330 −18.124	145.848 127.034	−16.338 −1.284	0.913 0.922
	m_3	0.126	0.006	0.255	-	CEDER PSA	101.927 86.357	7.143 −12.325	136.499 116.862	−19.155 −1.599	0.923 0.935
	m_6	0.094	0.001	0.038	0.301	CEDER PSA	101.762 85.478	8.770 −11.117	136.903 115.844	−20.294 −1.799	0.923 0.936

[1] $\mu mol\ m^{-1}\ s^{-1}$.

The regression analysis between the measured and estimated PAR showed that the MAE is much lower for the G1. The analysis of the bias errors (MBE) shows that the models overestimate in the case of the CEDER station, while they underestimate for the PSA data. The lowest MBEs are found with the CEDER data and the estimates from the G1 group models (Table 1). This bias between the two stations may be due to systematic differences; for example, in the equipment used in the measurement campaign.

In the case of the mean percentage error (MPE), the values obtained are low and close to 0%. Furthermore, the MPEs with CEDER data and those obtained with the PSA are even lower for the models of group G1 compared to those of G2.

As for the correlation coefficient of the different models, it can be seen that it is very close, high in all cases, highlighting that the highest values are obtained in the case of the G1 models (better results than the thousandth for CEDER). Regarding the G2 group, the results obtained (according to R^2) in the PSA are better than those provided by the CEDER station.

The mathematical expressions obtained and statistical results for each of the models developed can be consulted in Appendix A. To approach the analysis from a graphical point of view, the models m_1, m_3, and m_6 are shown in the following graphs (the statistical results for all models can be consulted in Appendix A as well). Figure 8 illustrates the scatterplots between the PAR estimated from the complete models and the PAR measured for the models m_1, m_3, and m_6 at both stations. On the one hand, it is clearly seen that the models that include k_t as an explanatory variable have a better fit for low PAR values at both locations. On the other hand, the models of group G2 show a remarkable dispersion, not only with low PAR values but also with medium and high PAR values. This is generalized when we look at all the dispersion curves of all the models studied.

In Figure 9, the Box–Whisker plot of the distribution of the absolute errors, Equation (11), for each model and test location, provides a visual representation of the goodness of the six models presented. The median, lower, and upper quartiles and any atypical values were displayed in this figure. On the one hand, it is clearly seen how the G1 models present a very narrow interquartile range around the absolute error value “0” (median value) and atypical values that are not very dispersed in both locations. On the other hand, when comparing the absolute error distributions of the two model types, it is observed that interval modeling gives better PAR estimation results than the complete models. This is noted by an even narrower interquartile range and fewer values considered as outliers.

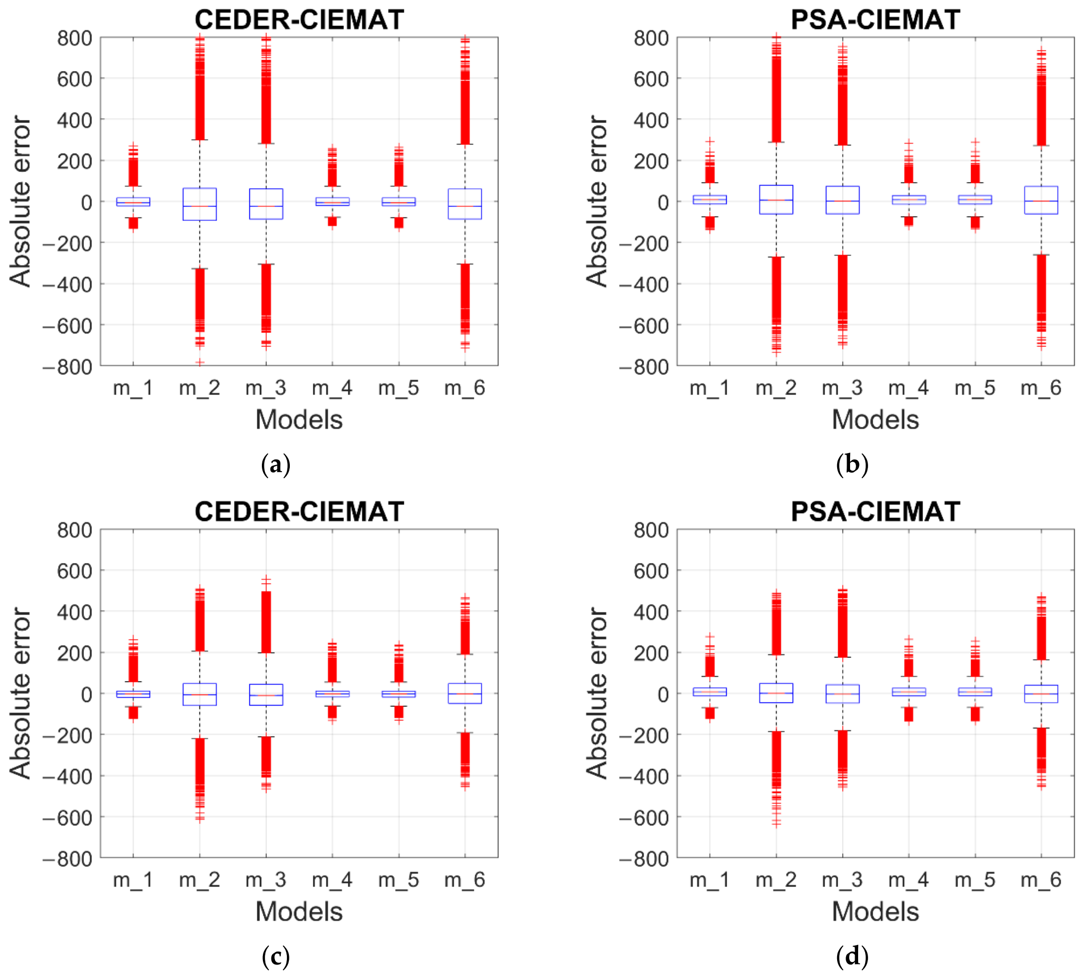

Figure 9. Absolute error distribution of the complete models (**a**,**b**) and interval models (**c**,**d**) proposed in Table 1 at the CEDER-CIEMAT (**a**,**c**) and PSA-CIEMAT (**b**,**d**) stations.

3.3. Comparison between Complete Models and Bibliographic Models

Comparing the statistics obtained at both stations (Table 2), all R^2 were high with slightly higher values at CEDER-CIEMAT. On the contrary, the MPEs were closer to zero at PSA-CIEMAT. Regarding the RMSE, models obtained better results at CEDER-CIEMAT, except for Alados et al. (1996) [29]. The MBE showed remarkable differences between both sites. For instance, the model result of Alados et al. (1996) at PSA-CIEMAT was two orders of magnitude lower than at CEDER-CIEMAT. Finally, all models, except Wang et al. (2015) [46], had a lower MAE at CEDER-CIEMAT.

Taking into account all statistics, models m_1, m_4, and m_5 had similar performance and lower statistics values. Among the models from the bibliography, it is noticeable that Alados et al. (1996) model presented the lower MPE and MBE of all models, including the models m_1, m_4, and m_5, at PSA-CIEMAT. At this station, Alados et al. (1996) obtained the best statistics, except for the MAE where Wang et al. (2015) had a lower value. In the case of CEDER-CIEMAT, Wang et al. (2015) model was the one that had the best statistics among the models from the bibliography [29,33,46,47].

In general, these results are not surprising because the models developed in this study were trained with data collected from these two stations. Given the importance of the climatic and atmospheric conditions in the behavior of PAR, the data used to develop the PAR models condition their performance when using data from other locations with very different climates. In this sense, the good results of the Alados et al. (2015) model in PSA-CIEMAT are explained because this model was trained using data from the University of Almería, where there is an arid climate influenced by the close presence of the sea, which is very similar to the climate of PSA-CIEMAT (both locations are approximately 40 km away).

Table 2. Statistical indices between complete models and literature models.

	CEDER-CIEMAT					PSA-CIEMAT				
Models	**MAE [1]**	**MBE [1]**	**RMSE [1]**	**MPE(%)**	**R^2**	**MAE [1]**	**MBE [1]**	**RMSE [1]**	**MPE(%)**	**R^2**
m_1	25.6828	3.242	33.425	1.795	0.995	28.445	−6.253	36.641	1.246	0.994
m_4	25.3128	2.542	33.177	−1.816	0.996	28.913	−6.040	37.433	1.186	0.994
m_5	25.5951	2.990	33.360	−1.851	0.995	28.673	−6.152	36.979	1.226	0.994
Alados	110.944	110.581	136.863	−15.840	0.994	116.581	5.819	53.018	1.125	0.992
Foyo-Moreno	110.0813	109.323	150.393	−12.479	0.994	124.593	123.633	166.398	−10.524	0.991
Wang	43.4608	36.287	53.859	−8.035	0.994	40.835	27.326	56.229	−2.993	0.991
Ferrera-Cobos	136.1521	135.026	174.649	−16.660	0.994	151.318	148.399	193.599	−12.384	0.991

[1] $\mu mol\ m^{-1}\ s^{-1}$.

3.4. Comparison between Complete Models and Interval Models

To improve the result with the complete model, the study was trained for intervals. For a given model, the estimated PAR is the set of overcast, partially overcast, and clear-sky estimates. Figure 10 shows the correlation graphs between the overall PAR estimated from the models and the PAR measured at each radiometric station. The validation statistics show an improvement in the estimated PAR data compared to those obtained from the complete models. It is clear that the models that include k_t as an explanatory variable have a better fit for low PAR values at both locations. However, the dispersion deviates slightly downward from the perfect correlation line at high PAR values.

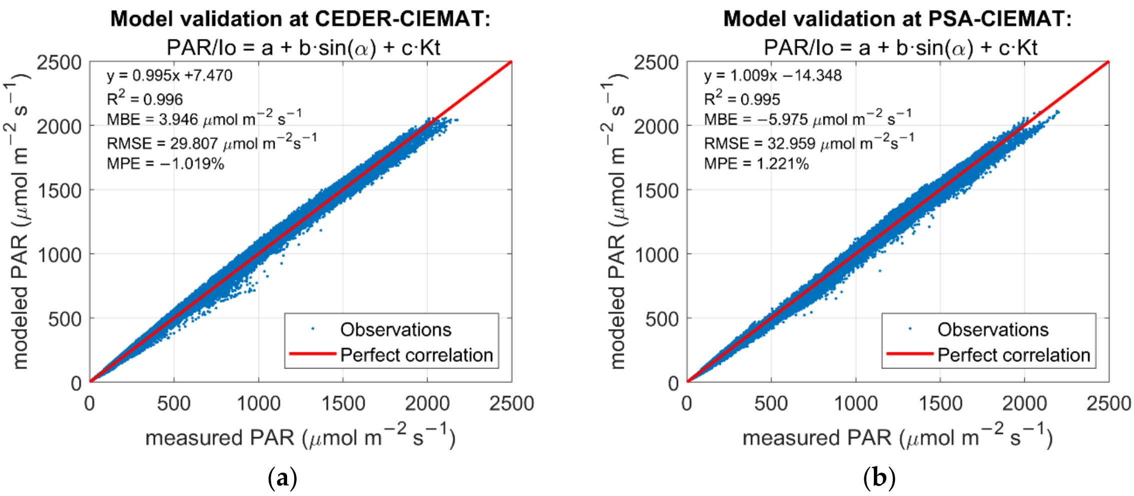

Figure 10. *Cont.*

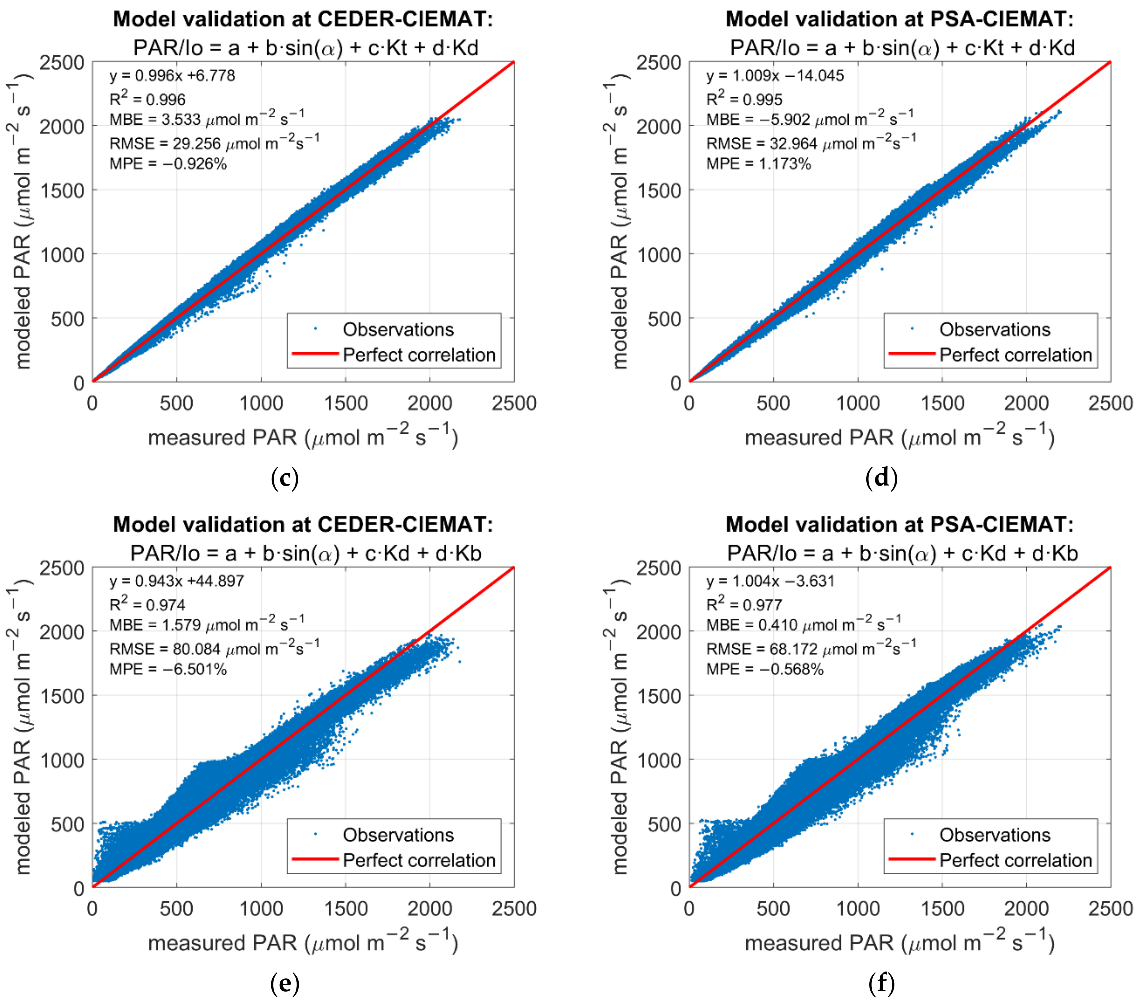

Figure 10. Results obtained in the validation of the interval models indicated above each graph using data measured at the CEDER-CIEMAT (**a**,**c**,**e**) and PSA-CIEMAT (**b**,**d**,**f**) stations.

4. Conclusions

The G1 models (m_1, m_4, and m_5), i.e., those that simultaneously include the atmospheric clearness index and the sine of the solar elevation angle as independent variables, present the best results, and it is difficult to discern which model is the best among them. Moreover, the bias errors calculated for both stations show that the models overestimate in the case of the CEDER station, while they underestimate for the PSA data. In addition, the analysis presented leads us to conclude that the model validation statistics indicate a better performance of the interval models than the complete models. The latter presented good results compared to the models found in the bibliography.

Conversely, the establishment of an improved PAR model could be based on minimizing systematic errors related to the measurement data in order to explore possible applications in other fields such as the calculation of energy balance in ecosystems or biomass productivity.

Author Contributions: Conceptualization, R.X.V. and L.F.Z.; methodology, R.X.V., L.F.Z., J.A.R.C. and O.W.; software, J.A.R.C. and O.W.; validation, J.A.R.C. and O.W.; formal analysis, L.F.Z., J.A.R.C. and O.W.; investigation, R.X.V., J.A.R.C. and O.W.; resources, R.X.V. and L.F.Z.; data curation, O.W., J.A.R.C., R.X.V., A.A.N., L.F.Z. and F.F.-C.; writing—original draft preparation, O.W., J.A.R.C., R.X.V., A.A.N., L.F.Z. and F.F.-C.; writing—review and editing, O.W., J.A.R.C., R.X.V., A.A.N., L.F.Z. and F.F.-C.; visualization, O.W., A.A.N., F.F.-C., R.X.V. and L.F.Z.; supervision, R.X.V. and L.F.Z.; project administration, R.X.V. and L.F.Z.; funding acquisition, R.X.V. All authors have read and agreed to the published version of the manuscript.

Funding: This research was funded by the Autonomous Community of Madrid, Spain, and was cofinanced by FEDER 'A way of making Europe' ALGATEC-CM (S2018/BAA-4532).

Data Availability Statement: Measured data belonging to Solar Radiation Group (CIEMAT) are available to bona fide researchers, subject to an agreement. For further details of the data and how to request access, contact the corresponding author.

Acknowledgments: The authors would like to thank the funding from the Autonomous Community of Madrid, Spain, and the cofinancing by FEDER 'A way of making Europe' ALGATEC-CM (S2018/BAA-4532). The authors also acknowledge the CYTED-IberoAmerican Program on Science and Technology for Development (RED RENUWAL P320RT0005 CYTED).

Conflicts of Interest: The authors declare that they have no conflict of interest.

Appendix A

Table A1. Model mathematical equations, results of the fits, and statistical validation of complete models.

Model	a	b	c	d	e	Station	MPE (%)	MBE [1]	RMSE [1]	R^2
$\frac{PAR}{I_0} = a + b \cdot \sin(\alpha)$	0.189	0.109	-	-	-	CEDER PSA	−69.046 −12.277	151.513 6.877	356.347 232.068	0.557 0.740
$\frac{PAR}{I_0} = a + b \cdot k_t$	0.007	0.372	-	-	-	CEDER PSA	−2.114 1.437	10.983 −1.049	35.786 44.151	0.996 0.994
$\frac{PAR}{I_0} = a + b \cdot k_d$	0.318	−0.204	-	-	-	CEDER PSA	−17.194 −1.731	−1.998 −25.528	147.847 128.259	0.911 0.921
$\frac{PAR}{I_0} = a + b \cdot k_b$	0.128	0.256	-	-	-	CEDER PSA	−19.24 −1.652	5.498 −13.661	136.714 116.63	0.924 0.935
$\frac{PAR}{I_0} = a + b \cdot \sin(\alpha) + c \cdot k_t$	0.018	−0.030	0.385	-	-	CEDER PSA	−1.795 1.246	3.242 −6.253	33.425 36.641	0.995 0.994
$\frac{PAR}{I_0} = a + b \cdot \sin(\alpha) + c \cdot k_d$	0.295	0.035	−0.198	-	-	CEDER PSA	−16.338 −1.284	6.33 −18.124	145.848 127.034	0.913 0.922
$\frac{PAR}{I_0} = a + b \cdot \sin(\alpha) + c \cdot k_b$	0.125	0.006	0.254	-	-	CEDER PSA	−19.155 −1.599	7.143 −12.325	136.499 116.862	0.923 0.935
$\frac{PAR}{I_0} = a + b \cdot k_t + c \cdot k_d$	0.025	0.353	−0.014	-	-	CEDER PSA	−2.15 1.296	9.442 −0.789	34.877 44.92	0.996 0.993
$\frac{PAR}{I_0} = a + b \cdot k_t + c \cdot k_b$	0.009	0.365	0.006	-	-	CEDER PSA	−2.206 1.394	10.633 −0.802	35.49 44.623	0.996 0.993
$\frac{PAR}{I_0} = a + b \cdot k_d + c \cdot k_b$	0.093	0.039	0.303	-	-	CEDER PSA	−20.343 −1.812	8.661 −11.213	136.944 115.783	0.923 0.936
$\frac{PAR}{I_0} = a + b \cdot \sin(\alpha) + c \cdot k_t + d \cdot k_d$	0.028	−0.029	0.373	−0.008	-	CEDER PSA	−1.816 1.186	2.542 −6.04	33.177 37.433	0.996 0.994
$\frac{PAR}{I_0} = a + b \cdot \sin(\alpha) + c \cdot k_t + d \cdot k_b$	0.019	−0.030	0.380	0.004	-	CEDER PSA	−1.851 1.226	2.99 −6.152	33.36 36.979	0.995 0.994
$\frac{PAR}{I_0} = a + b \cdot \sin(\alpha) + c \cdot k_d + d \cdot k_b$	0.094	0.001	0.038	0.301	-	CEDER PSA	−20.294 −1.799	8.77 −11.117	136.903 115.844	0.923 0.936
$\frac{PAR}{I_0} = a + b \cdot k_t + c \cdot k_d + d \cdot k_b$	0.073	0.373	−0.072	−0.087	-	CEDER PSA	−1.070 1.310	8.825 −3.016	35.513 41	0.996 0.993
$\frac{PAR}{I_0} = a + b \cdot \sin(\alpha) + c \cdot k_t + d \cdot k_d + e \cdot k_b$	0.056	−0.025	0.383	−0.044	−0.053	CEDER PSA	−1.165 1.200	3.082 -6.521	33.085 36.047	0.996 0.994

[1] $\mu mol\ m^{-1}\ s^{-1}$.

Table A2. Model mathematical equations and results of the fits of interval models.

	Cloudy Skies ($0 \leq \mathbf{k_t} \leq 0.3$)					**Partly Cloudy Skies** ($0.3 < \mathbf{k_t} \leq 0.7$)					**Clear Skies** ($0.7 < \mathbf{k_t} \leq 1$)				
Model	**a**	**b**	**c**	**d**	**e**	**a**	**b**	**c**	**d**	**e**	**a**	**b**	**c**	**d**	**e**
$\frac{PAR}{I_0} = a + b \cdot \sin(\alpha)$	0.068	0.021				0.218	−0.001				0.311	−0.022			
$\frac{PAR}{I_0} = a + b \cdot k_t$	0.003	0.378				−0.003	0.400				0.045	0.321			
$\frac{PAR}{I_0} = a + b \cdot k_d$	0.143	−0.067				0.275	−0.124				0.291	0.027			
$\frac{PAR}{I_0} = a + b \cdot k_b$	0.077	0.171				0.157	0.182				0.287	0.014			
$\frac{PAR}{I_0} = a + b \cdot \sin(\alpha) + c \cdot k_t$	0.002	0.001	0.377			0.006	−0.021	0.402			0.051	−0.042	0.351		
$\frac{PAR}{I_0} = a + b \cdot \sin(\alpha) + c \cdot k_d$	0.143	0.026	−0.080			0.264	0.028	−0.128			0.306	−0.020	0.022		
$\frac{PAR}{I_0} = a + b \cdot \sin(\alpha) + c \cdot k_b$	0.065	0.026	0.213			0.147	0.020	0.185			0.297	−0.026	0.028		
$\frac{PAR}{I_0} = a + b \cdot k_t + c \cdot k_d$	0.012	0.376	−0.009			0.025	0.366	−0.019			0.045	0.318	0.014		
$\frac{PAR}{I_0} = a + b \cdot k_t + c \cdot k_b$	0.003	0.377	0.012			0.009	0.362	0.027			0.053	0.331	−0.024		
$\frac{PAR}{I_0} = a + b \cdot k_d + c \cdot k_b$	0.194	−0.119	−0.164			0.059	0.108	0.329			0.059	0.261	0.304		
$\frac{PAR}{I_0} = a + b \cdot \sin(\alpha) + c \cdot k_t + d \cdot k_d$	0.012	0.002	0.374	−0.010		0.023	−0.016	0.377	−0.013		0.051	−0.041	0.350	0.003	
$\frac{PAR}{I_0} = a + b \cdot \sin(\alpha) + c \cdot k_t + d \cdot k_b$	0.002	0.001	0.372	0.015		0.013	−0.016	0.374	0.020		0.052	−0.041	0.353	−0.005	
$\frac{PAR}{I_0} = a + b \cdot \sin(\alpha) + c \cdot k_d + d \cdot k_b$	0.180	0.026	−0.118	−0.118		0.063	0.012	0.096	0.315		0.026	−0.049	0.319	0.394	
$\frac{PAR}{I_0} = a + b \cdot k_t + c \cdot k_d + d \cdot k_b$	0.053	0.375	−0.051	−0.132		0.026	0.367	−0.020	−0.002		0.087	0.395	−0.091	−0.133	
$\frac{PAR}{I_0} = a + b \cdot \sin(\alpha) + c \cdot k_t + d \cdot k_d + e \cdot k_b$	0.053	0.001	0.374	−0.051	−0.129	0.019	−0.016	0.376	−0.008	0.008	0.058	−0.040	0.364	−0.016	−0.025

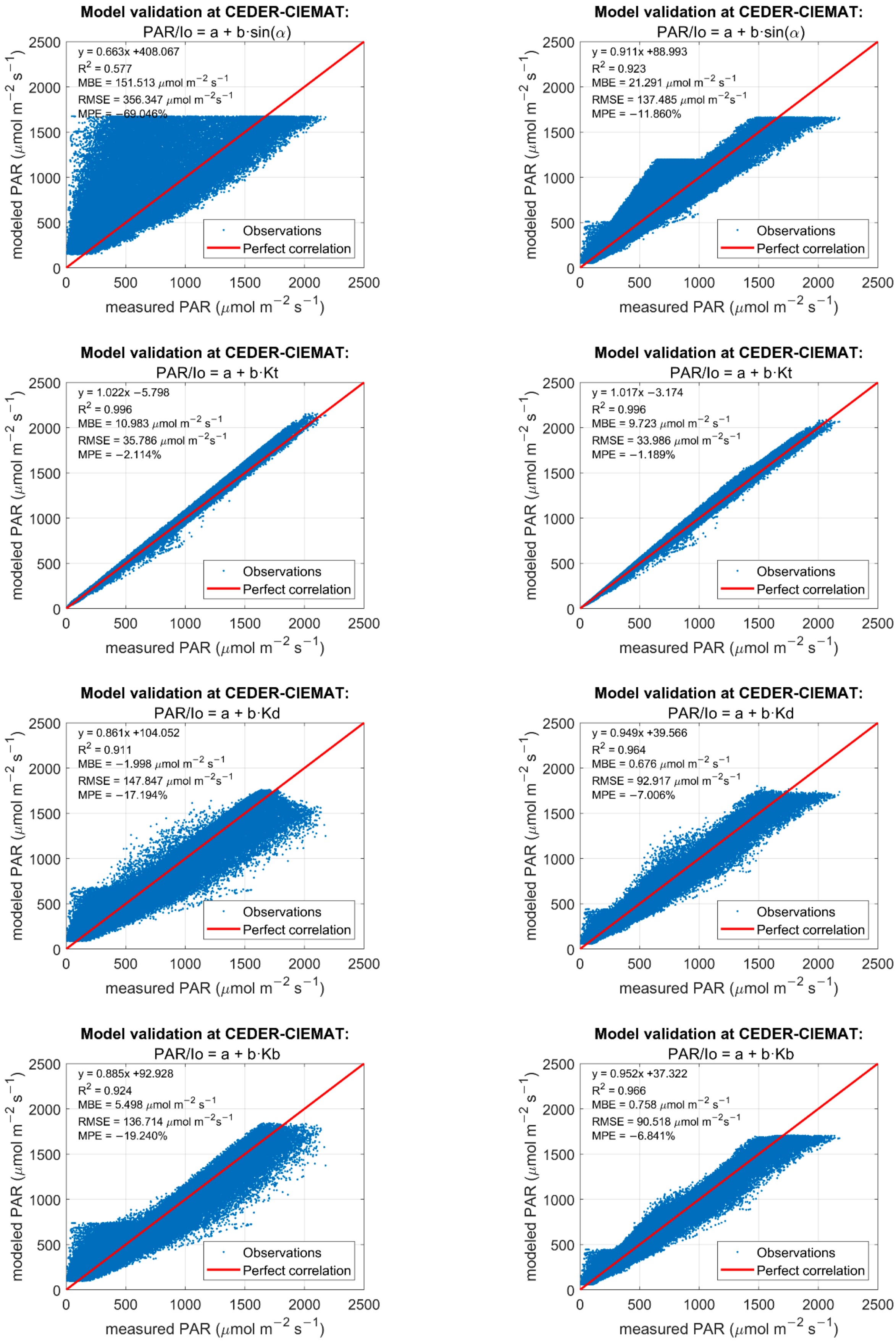

Figure A1. *Cont.*

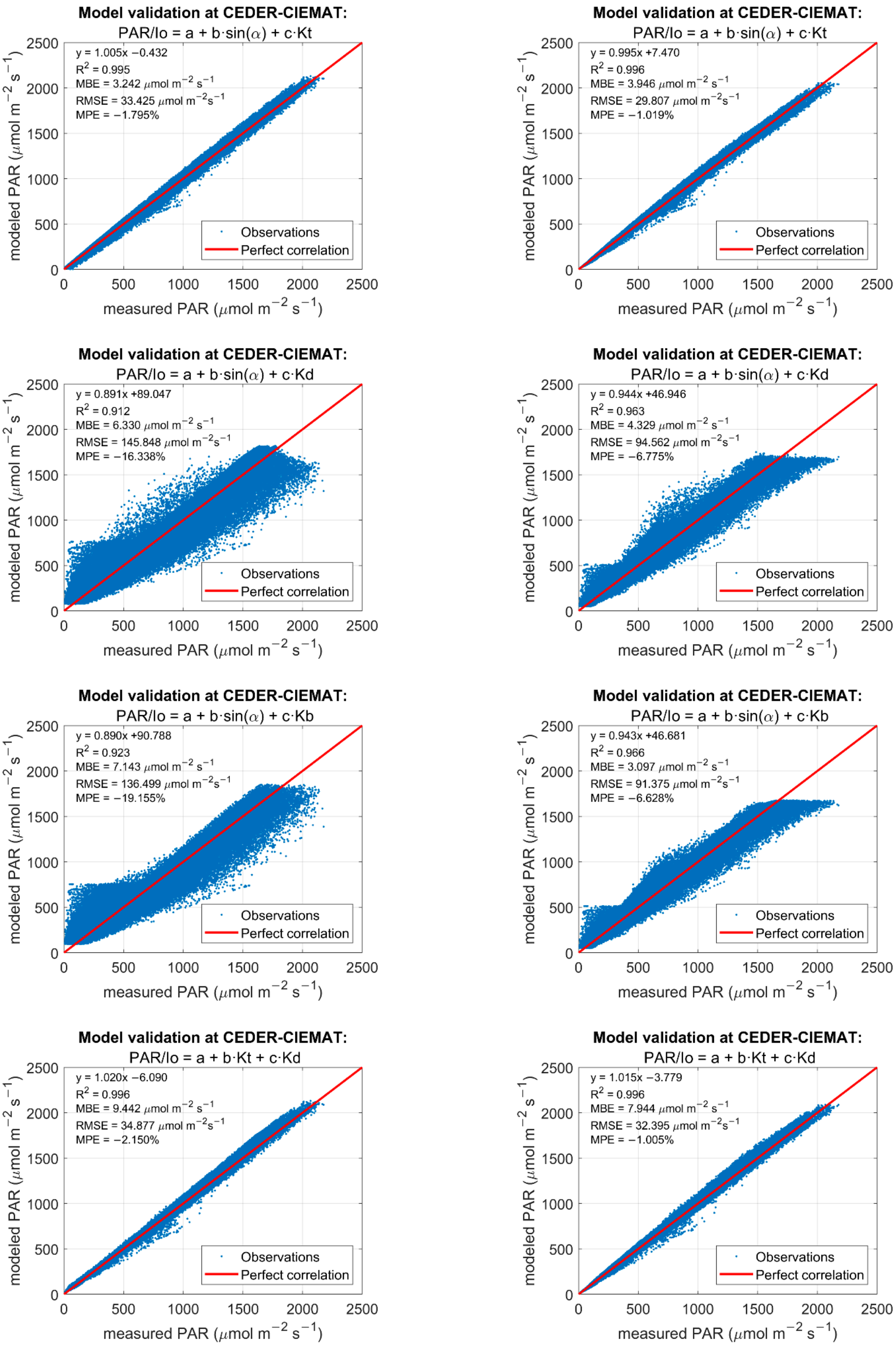

Figure A1. *Cont.*

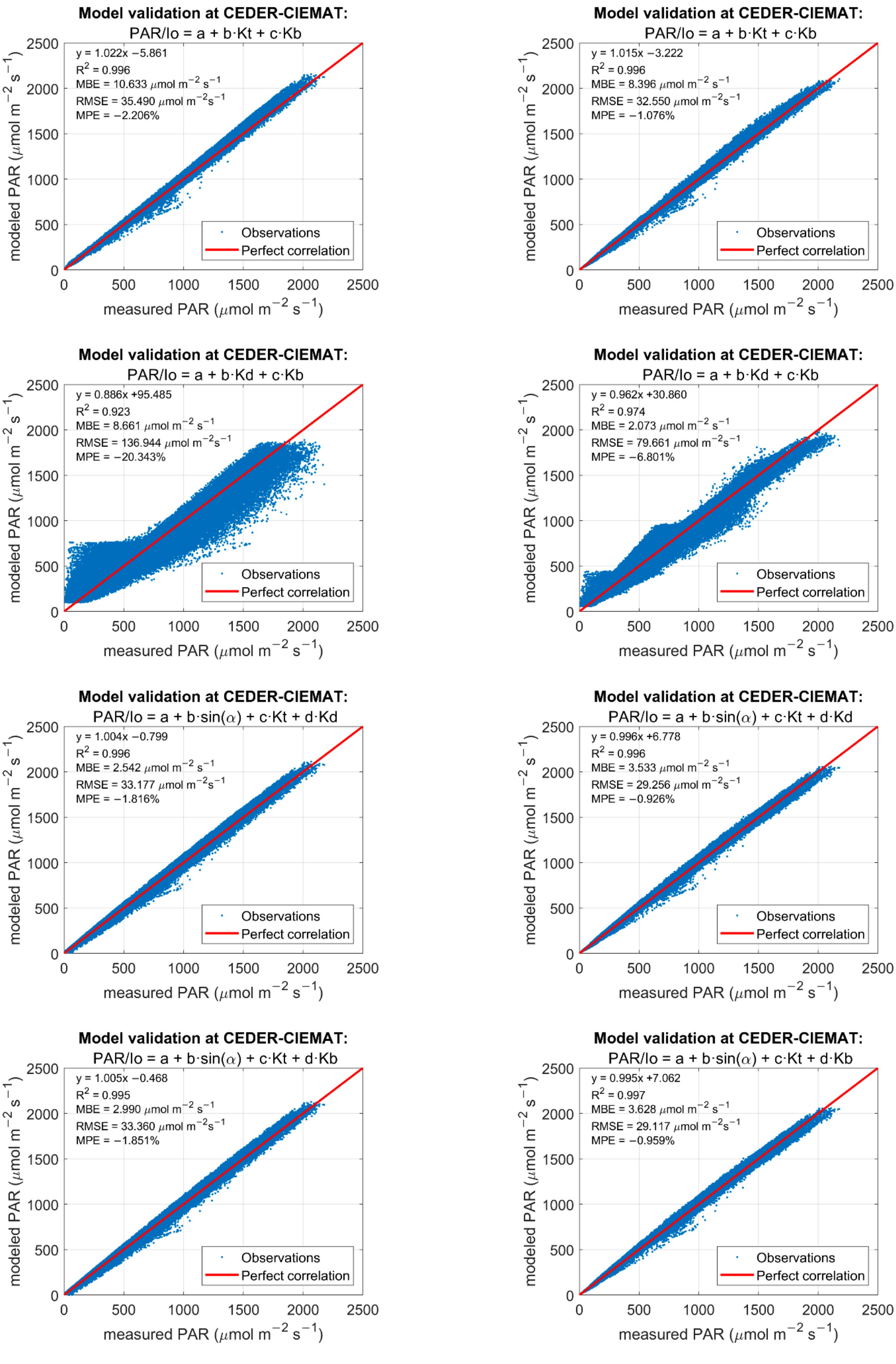

Figure A1. *Cont.*

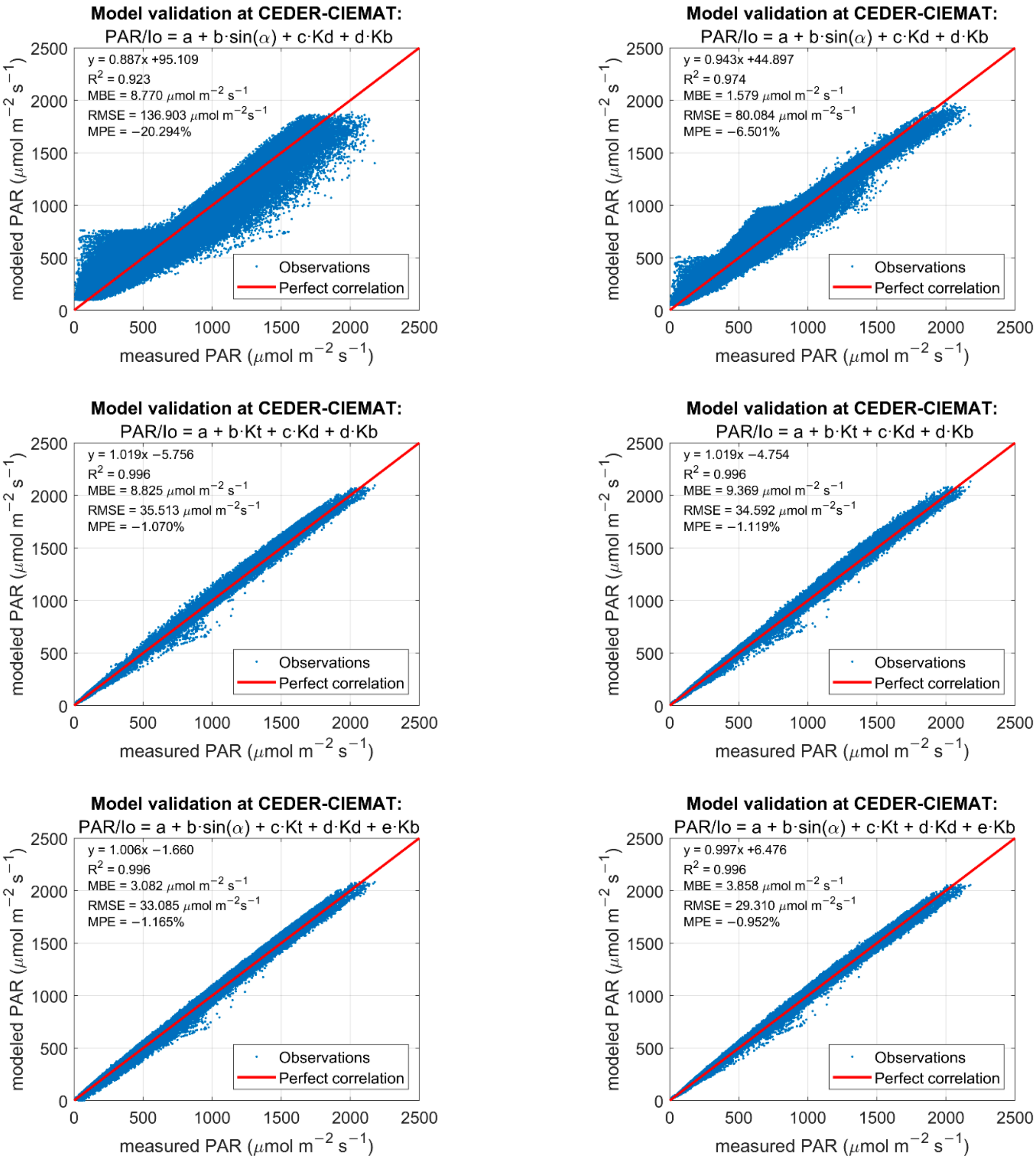

Figure A1. Results obtained in the validation of all 15 complete (first column) and interval (second column) models indicated above each graph using data provided by the CEDER-CIEMAT stations.

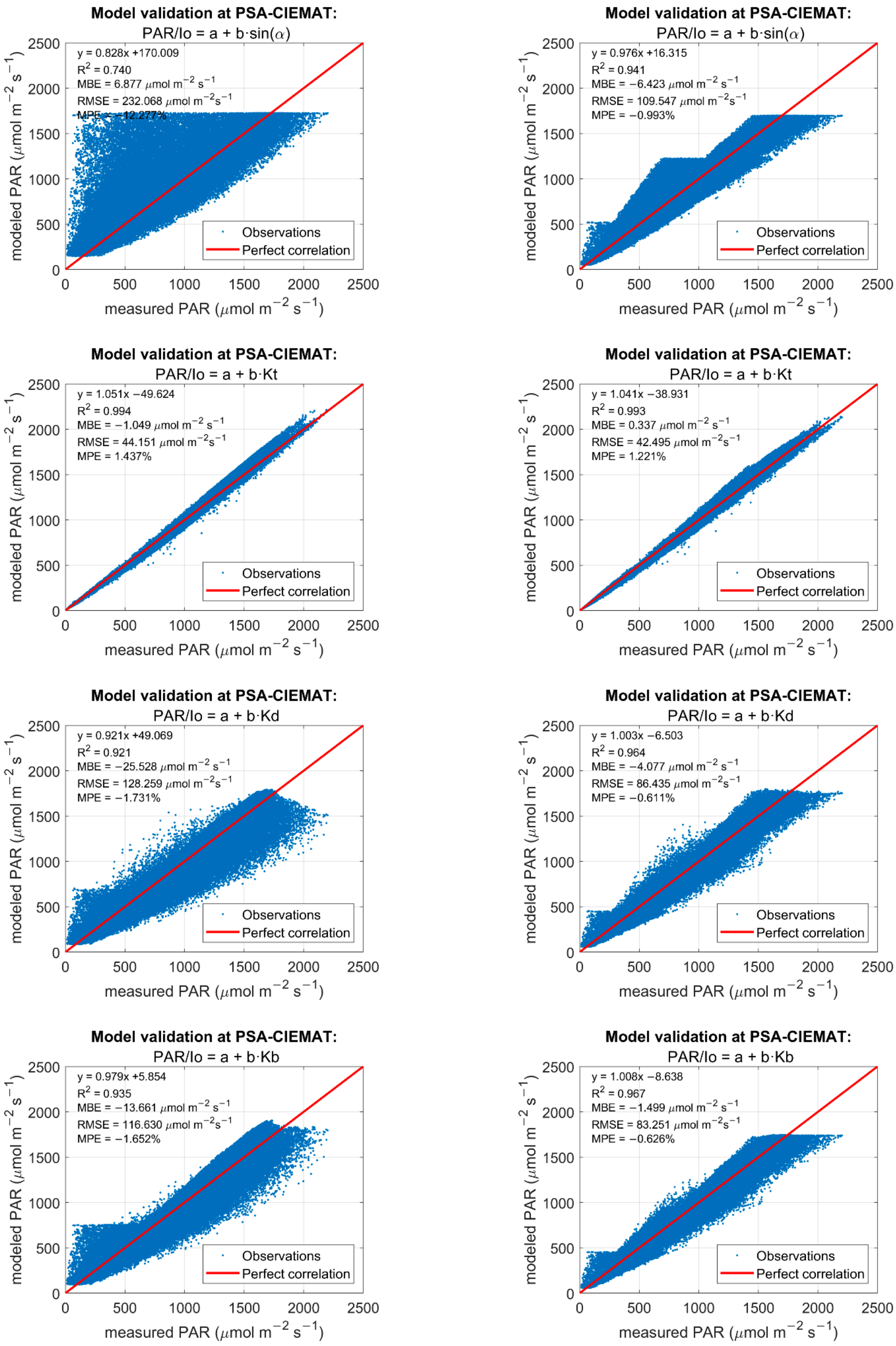

Figure A2. *Cont.*

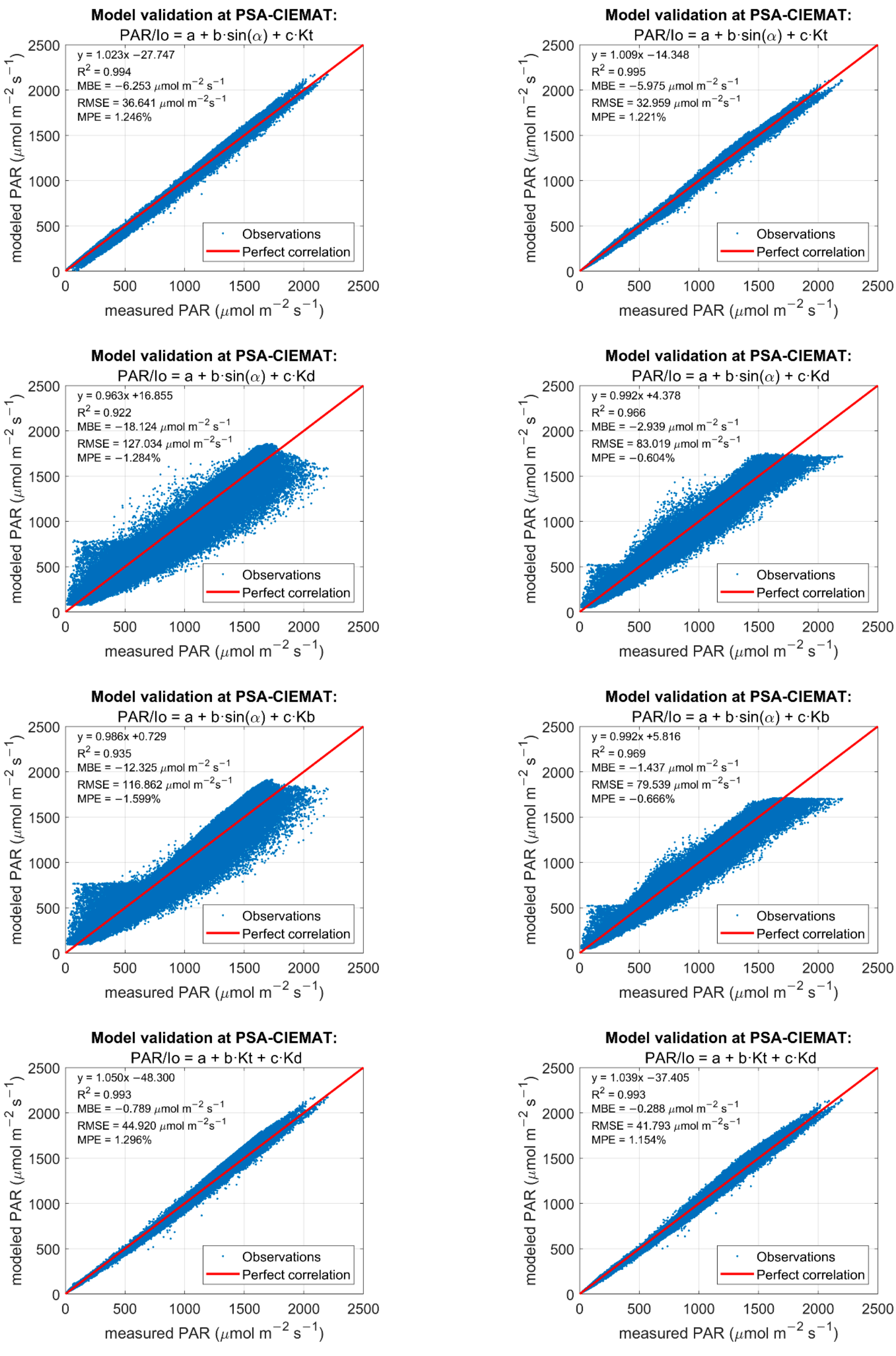

Figure A2. *Cont.*

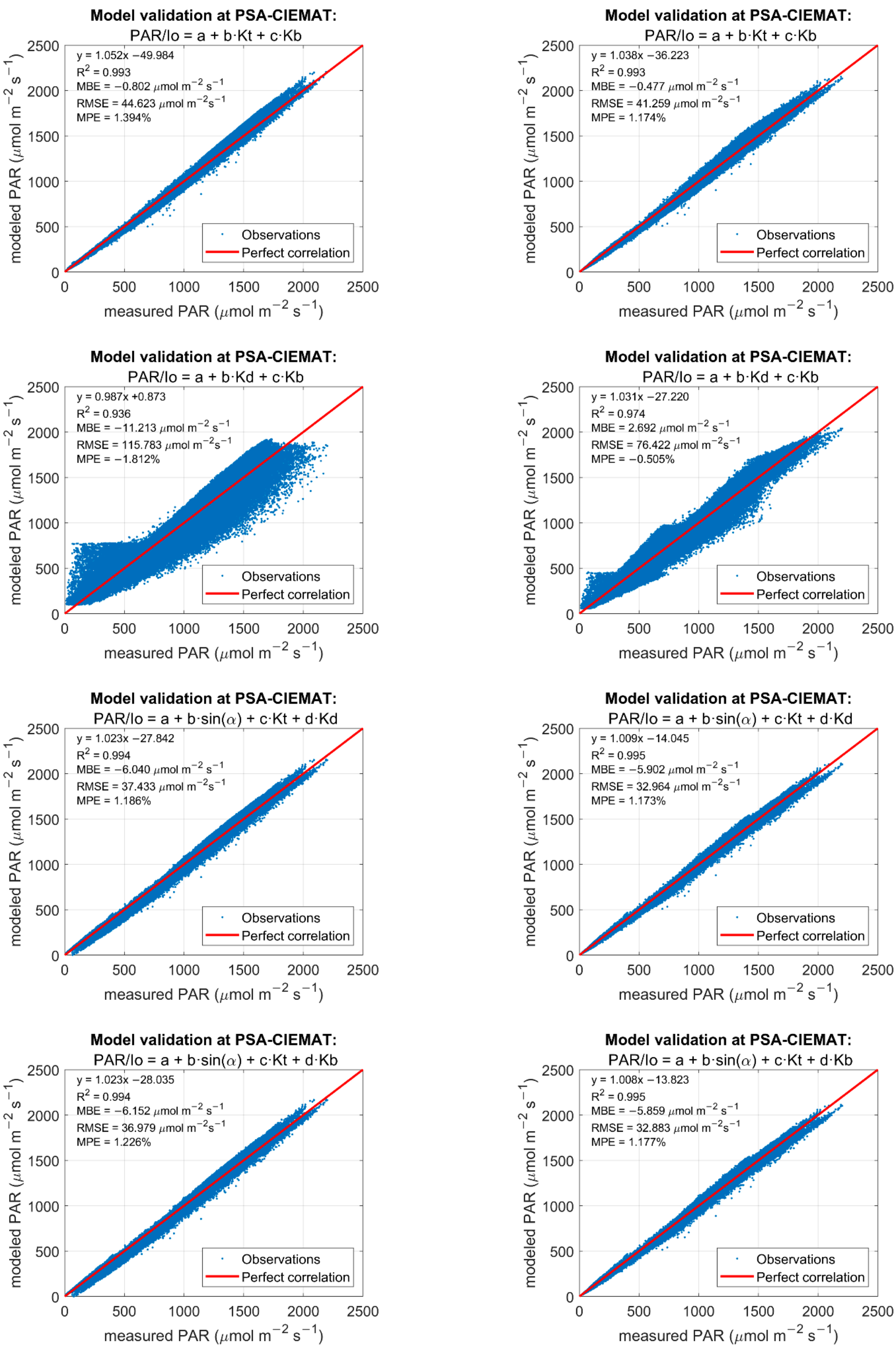

Figure A2. *Cont.*

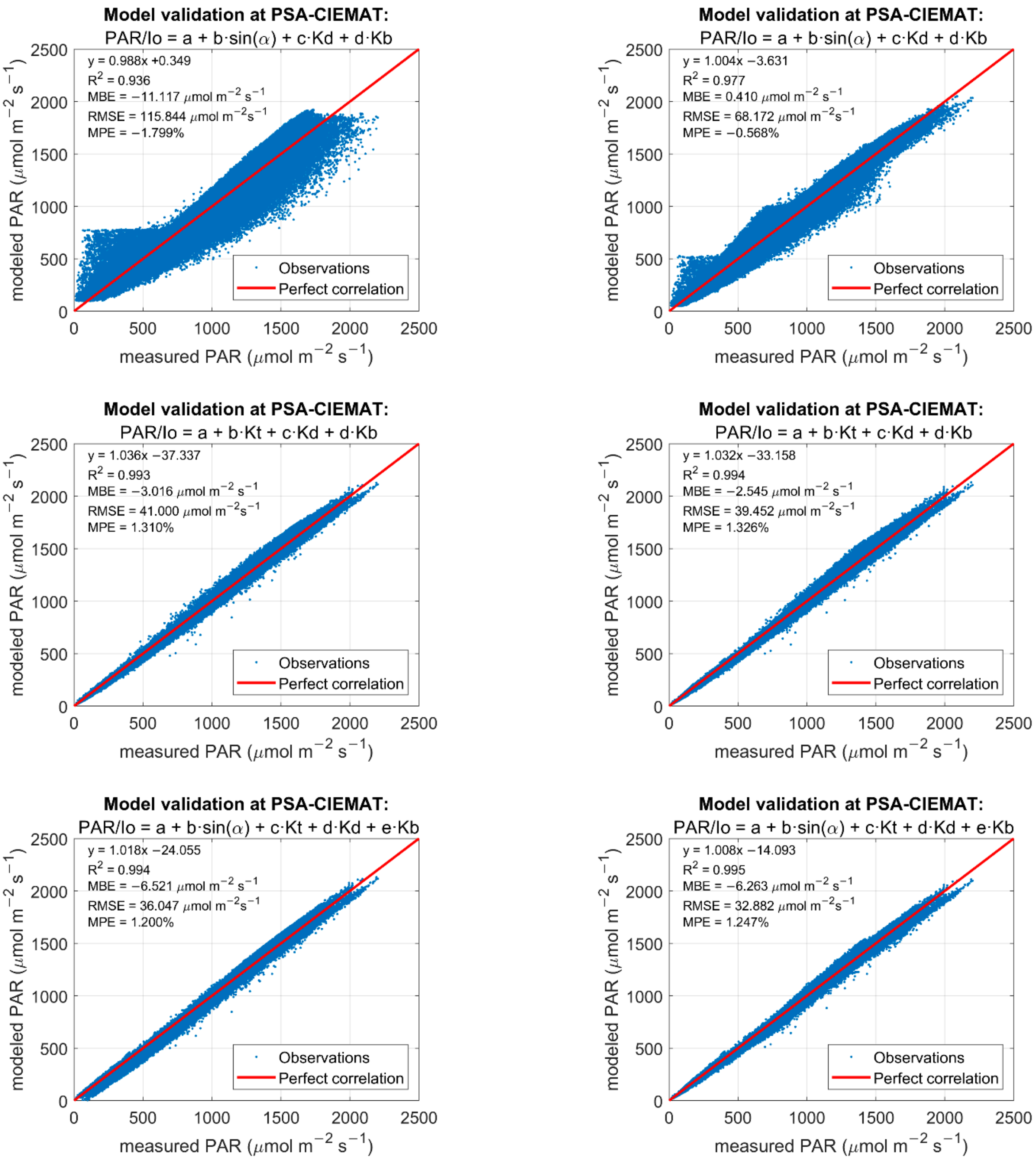

Figure A2. Results obtained in the validation of all 15 complete (first column) and interval (second column) models indicated above each graph using data provided by the PSA-CIEMAT stations.

References

1. Hindersin, S.; Leupold, M.; Kerner, M.; Hanelt, D. Key Parameters for Outdoor Biomass Production of Scenedesmus Obliquus in Solar Tracked Photobioreactors. *J. Appl. Phycol.* **2014**, *26*, 2315–2325. [CrossRef]
2. Raymond Hunt, E., Jr. Relationship between Woody Biomass and PAR Conversion Efficiency for Estimating Net Primary Production from NDVI. *Int. J. Remote Sens.* **1994**, *15*, 1725–1729. [CrossRef]
3. Ramírez-Pérez, L.J.; Morales-Díaz, A.B.; De Alba-Romenus, K.; González-Morales, S.; Benavides-Mendoza, A.; Juárez-Maldonado, A. Determination of Micronutrient Accumulation in Greenhouse Cucumber Crop Using a Modeling Approach. *Agronomy* **2017**, *7*, 79. [CrossRef]
4. Kim, T.H.; Lee, Y.; Han, S.H.; Hwang, S.J. The Effects of Wavelength and Wavelength Mixing Ratios on Microalgae Growth and Nitrogen, Phosphorus Removal Using *Scenedesmus* Sp. for Wastewater Treatment. *Bioresour. Technol.* **2013**, *130*, 75–80. [CrossRef]
5. Trofimchuk, O.A.; Petikar, P.V.; Turanov, S.B.; Romanenko, S.A. The Influence of PAR Irradiance on Yield Growth of Chlorella Microalgae. *IOP Conf. Ser. Mater. Sci. Eng.* **2019**, *510*. [CrossRef]

6. Schmidt, J.J.; Gagnon, G.A.; Jamieson, R.C. Microalgae Growth and Phosphorus Uptake in Wastewater under Simulated Cold Region Conditions. *Ecol. Eng.* **2016**, *95*, 588–593. [CrossRef]
7. Vadiveloo, A.; Moheimani, N.R.; Cosgrove, J.J.; Bahri, P.A.; Parlevliet, D. Effect of Different Light Spectra on the Growth and Productivity of Acclimated *Nannochloropsis* Sp. (Eustigmatophyceae). *Algal Res.* **2015**, *8*, 121–127. [CrossRef]
8. Prasad, R.; Gupta, S.K.; Shabnam, N.; Oliveira, C.Y.B.; Nema, A.K.; Ansari, F.A.; Bux, F. Role of Microalgae in Global CO_2 Sequestration: Physiological Mechanism, Recent Development, Challenges, and Future Prospective. *Sustainability* **2021**, *13*, 13061. [CrossRef]
9. Farrelly, D.J.; Everard, C.D.; Fagan, C.C.; McDonnell, K.P. Carbon Sequestration and the Role of Biological Carbon Mitigation: A Review. *Renew. Sustain. Energy Rev.* **2013**, *21*, 712–727. [CrossRef]
10. Ali, H.; Park, C.W. Numerical Multiphase Modeling of CO_2 Absorption and Desorption in Microalgal Raceway Ponds to Improve Their Carbonation Efficiency. *Energy* **2017**, *127*, 358–371. [CrossRef]
11. Wu, C.; Niu, Z.; Tang, Q.; Huang, W.; Rivard, B.; Feng, J. Remote Estimation of Gross Primary Production in Wheat Using Chlorophyll-Related Vegetation Indices. *Agric. For. Meteorol.* **2009**, *149*, 1015–1021. [CrossRef]
12. Pinker, R.T.; Zhao, M.; Wang, H.; Wood, E.F. Impact of Satellite Based PAR on Estimates of Terrestrial Net Primary Productivity. *Int. J. Remote Sens.* **2010**, *31*, 5221–5237. [CrossRef]
13. Leblon, B.; Guerif, M.; Baret, F. The Use of Remotely Sensed Data in Estimation of PAR Use Efficiency and Biomass Production of Flooded Rice. *Remote Sens. Environ.* **1991**, *38*, 147–158. [CrossRef]
14. Gu, L.; Baldocchi, D.; Verma, S.B.; Black, T.A.; Vesala, T.; Falge, E.M.; Dowty, P.R. Advantages of Diffuse Radiation for Terrestrial Ecosystem Productivity. *J. Geophys. Res. Atmos.* **2002**, *107*, ACL-2. [CrossRef]
15. Roderick, M.L.; Farquhar, G.D.; Berry, S.L.; Noble, I.R. On the Direct Effect of Clouds and Atmospheric Particles on the Productivity and Structure of Vegetation. *Oecologia* **2001**, *129*, 21–30. [CrossRef]
16. Lee, C.-s.; Hoes, P.; Cóstola, D.; Hensen, J.L.M. Assessing the Performance Potential of Climate Adaptive Greenhouse Shells. *Energy* **2019**, *175*, 534–545. [CrossRef]
17. Cemek, B.; Demir, Y.; Uzun, S.; Ceyhan, V. The Effects of Different Greenhouse Covering Materials on Energy Requirement, Growth and Yield of Aubergine. *Energy* **2006**, *31*, 1780–1788. [CrossRef]
18. Wang, C.; Du, J.; Liu, Y.; Chow, D. A Climate-Based Analysis of Photosynthetically Active Radiation Availability in Large-Scale Greenhouses across China. *J. Clean. Prod.* **2021**, *315*, 127901. [CrossRef]
19. Wang, L.; Gong, W.; Lin, A.; Hu, B. Analysis of Photosynthetically Active Radiation under Various Sky Conditions in Wuhan, Central China. *Int. J. Biometeorol.* **2014**, *58*, 1711–1720. [CrossRef]
20. Wang, L.; Gong, W.; Ma, Y.; Hu, B.; Zhang, M. Photosynthetically Active Radiation and Its Relationship with Global Solar Radiation in Central China. *Int. J. Biometeorol.* **2014**, *58*, 1265–1277. [CrossRef]
21. Ferrera-Cobos, F.; Vindel, J.M.; Valenzuela, R.X.; González, J.A. Analysis of Spatial and Temporal Variability of the PAR/GHI Ratio and PAR Modeling Based on Two Satellite Estimates. *Remote Sens.* **2020**, *12*, 1262. [CrossRef]
22. Akitsu, T.K.; Nasahara, K.N.; Ijima, O.; Hirose, Y.; Ide, R.; Takagi, K.; Kume, A. The Variability and Seasonality in the Ratio of Photosynthetically Active Radiation to Solar Radiation: A Simple Empirical Model of the Ratio. *Int. J. Appl. Earth Obs. Geoinf.* **2022**, *108*, 102724. [CrossRef]
23. Xia, X.; Li, Z.; Wang, P.; Chen, H.; Cribb, M. Estimation of Aerosol Effects on Surface Irradiance Based on Measurements and Radiative Transfer Model Simulations in Northern China. *J. Geophys. Res.* **2007**, *112*, D22S10. [CrossRef]
24. Kidder, S.Q.; Vonder Haar, T.H. *Satellite Meteorology—An Introduction*; Academic Press: Cambridge, MA, USA, 1995; ISBN 978-0124064300.
25. Ferrera-Cobos, F.; Vindel, J.M.; Valenzuela, R.X.; González, J.A. Models for Estimating Daily Photosynthetically Active Radiation in Oceanic and Mediterranean Climates and Their Improvement by Site Adaptation Techniques. *Adv. Sp. Res.* **2020**, *65*, 1894–1909. [CrossRef]
26. Vindel, J.M.; Valenzuela, R.X.; Navarro, A.A.; Zarzalejo, L.F.; Paz-Gallardo, A.; Souto, J.; Méndez-Gómez, R.; Cartelle, D.; Casares, J. Modeling Photosynthetically Active Radiation from Satellite-Derived Estimations over Mainland Spain. *Remote Sens.* **2018**, *10*, 849. [CrossRef]
27. Lozano, I.L.; Sánchez-Hernández, G.; Guerrero-Rascado, J.L.; Alados, I.; Foyo-Moreno, I. Analysis of Cloud Effects on Long-Term Global and Diffuse Photosynthetically Active Radiation at a Mediterranean Site. *Atmos. Res.* **2022**, *268*, 106010. [CrossRef]
28. Escobedo, J.F.; Gomes, E.N.; Oliveira, A.P.; Soares, J. Modeling Hourly and Daily Fractions of UV, PAR and NIR to Global Solar Radiation under Various Sky Conditions at Botucatu, Brazil. *Appl. Energy* **2009**, *86*, 299–309. [CrossRef]
29. Alados, I.; Foyo-Moreno, I.; Alados-Arboledas, L. Photosynthetically Active Radiation: Measurements and Modelling. *Agric. For. Meteorol.* **1996**, *78*, 121–131. [CrossRef]
30. Mizoguchi, Y.; Yasuda, Y.; Ohtani, Y.; Watanabe, T.; Kominami, Y.; Yamanoi, K. A Practical Model to Estimate Photosynthetically Active Radiation Using General Meteorological Elements in a Temperate Humid Area and Comparison among Models. *Theor. Appl. Climatol.* **2014**, *115*, 583–589. [CrossRef]
31. Yu, X.; Wu, Z.; Jiang, W.; Guo, X. Predicting Daily Photosynthetically Active Radiation from Global Solar Radiation in the Contiguous United States. *Energy Convers. Manag.* **2015**, *89*, 71–82. [CrossRef]
32. Pashiardis, S.; Kalogirou, S.; Pelengaris, A. Characteristics of Photosynthetic Active Radiation (PAR) Through Statistical Analysis at Larnaca, Cyprus. *SM J. Biometrics Biostat.* **2017**, *2*, 1–16. [CrossRef]

33. Ferrera-Cobos, F.; Vindel, J.M.; Valenzuela, R.X. A New Index Assessing the Viability of PAR Application Projects Used to Validate PAR Models. *Agronomy* **2021**, *11*, 470. [CrossRef]
34. García-Rodríguez, A.; Granados-López, D.; García-Rodríguez, S.; Díez-Mediavilla, M.; Alonso-Tristán, C. Modelling Photosynthetic Active Radiation (PAR) through Meteorological Indices under All Sky Conditions. *Agric. For. Meteorol.* **2021**, *310*, 108627. [CrossRef]
35. National Renewable Energy Laboratory. *Users Manual for SERf QC Software—Assessing the Quality of Solar Radiation*; National Renewable Energy Laboratory: Golden, CO, USA, 1993.
36. Sengupta, M.; Habte, A.; Kurtz, S.; Dobos, A.; Wilbert, S.; Lorenz, E.; Stoffel, T.; Renné, D.; Gueymard, C.; Myers, D.; et al. *Best Practices Handbook for the Collection and Use of Solar Resource Data for Solar Energy Applications*; IEA: Paris, France, 2015.
37. Liu, B.Y.H.; Jordan, R.C. The Interrelationship and Characteristic Distribution of Direct, Diffuse and Total Solar Radiation. *Sol. Energy* **1960**, *4*, 1–19. [CrossRef]
38. Köppen, W.; Geiger, R. *Das Geographische System Der Klimate*; Gebrüder, B., Ed.; Mit 14 Textflguren: Berlin, Germany, 1936.
39. Agencia Estatal de Meteorología (AEMET); Instituto de Meteorologia de Portugal (IM). *Atlas Climático Ibérico—Iberian Climate Atlas*; AEMET-Ministerio de Medio Ambiente, y Medio Rural y Marino & Instituto de Meteorologia de Portugal: Madrid, Spain, 2011.
40. Zo, I.S.; Jee, J.B.; Kim, B.Y.; Lee, K.T. Baseline Surface Radiation Network (BSRN) Quality Control of Solar Radiation Data on the Gangneung-Wonju National University Radiation Station. *Asia-Pacific J. Atmos. Sci.* **2017**, *53*, 11–19. [CrossRef]
41. Hu, B.; Wang, Y.; Liu, G. Spatiotemporal Characteristics of Photosynthetically Active Radiation in China. *J. Geophys. Res. Atmos.* **2007**, *112*, 1–12. [CrossRef]
42. Polo, J.; Zarzalejo, L.F.; Ramirez, L.; Espinar, B. Iterative Filtering of Ground Data for Qualifying Statistical Models for Solar Irradiance Estimation from Satellite Data. *Sol. Energy* **2006**, *80*, 240–247. [CrossRef]
43. Sengupta, M.; Habte, A.; Wilbert, S.; Gueymard, C.A.; Remund, J. *Best Practices Handbook for the Collection and Use of Solar Resource Data for Solar Energy Applications*; IEA: Paris, France, 2021.
44. Iqbal, M. *An Introduction to Solar Radiation*; Academic Press: Toronto, ON, USA, 1983; ISBN 0123737508/9780123737502/0123737524/9780123737526.
45. Salazar, G.; Raichijk, C. Evaluation of Clear-Sky Conditions in High Altitude Sites. *Renew. Energy* **2014**, *64*, 197–202. [CrossRef]
46. Wang, L.; Gong, W.; Hu, B.; Lin, A.; Li, H.; Zou, L. Modeling and Analysis of the Spatiotemporal Variations of Photosynthetically Active Radiation in China during 1961–2012. *Renew. Sustain. Energy Rev.* **2015**, *49*, 1019–1032. [CrossRef]
47. Foyo-Moreno, I.; Alados, I.; Alados-Arboledas, L. A New Conventional Regression Model to Estimate Hourly Photosynthetic Photon Flux Density under All Sky Conditions. *Int. J. Climatol.* **2017**, *37*, 1067–1075. [CrossRef]